Formulation, optimization and sensitivity of NitrOMZv1.0, a biogeochemical model of the nitrogen cycle in oceanic oxygen minimum zones

Daniele Bianchi[1], Daniel McCoy[1], and Simon Yang[1]

[1]University of California Los Angeles, CA

Correspondence: Daniele Bianchi (dbianchi@atmos.ucla.edu)

Abstract.

Nitrogen (N) plays a central role in marine biogeochemistry by limiting biological productivity in the surface ocean, influencing the cycles of other nutrients, carbon, and oxygen, and controlling oceanic emissions of nitrous oxide (N_2O) to the atmosphere. Multiple chemical forms of N are linked together in a dynamic N cycle that is especially active in oxygen mini-
5   mum zones (OMZs), where high organic matter remineralization and low oxygen concentrations fuel aerobic and anaerobic N transformations. Biogeochemical models used to understand the oceanic N cycle and project its change often employ simple parameterizations of the network of N transformations and omit key intermediary tracers such as nitrite (NO_2^-) and N_2O. Here we present a new model of the oceanic N cycle (**Nitr**ogen cycling in **O**xygen **M**inimum **Z**ones, or NitrOMZ) that resolves N transformation occurring within OMZs, and their sensitivity to environmental drivers. The model is designed to be easily
10   coupled to current ocean biogeochemical models by representing the major forms of N as prognostic tracers, and parameterizing their transformations as a function of seawater chemistry and organic matter remineralization, with minimal interference with other elemental cycles. We describe the model rationale, formulation, and numerical implementation in a one-dimensional representation of the water column that reproduces typical OMZ conditions. We further detail the optimization of uncertain model parameters against observations from the Eastern Tropical South Pacific OMZ, and evaluate the model ability to repro-
15   duce observed profiles of N tracers and transformation rates in this region. We conclude by describing the model sensitivity to parameter choices and environmental factors, and discussing the model suitability for ocean biogeochemical studies.

1 Introduction

Nitrogen (N) limits phytoplankton production over large swathes of the ocean (Moore et al., 2013). Most of the N in the ocean is present as dissolved dinitrogen gas (N_2); however, only fixed N, e.g., ammonium (NH_4^+) and nitrate (NO_3^-), can be readily utilized by planktonic microorganisms, with the exception of N-fixing diazotrophs (Capone et al., 2008). The inventory and chemical form of N in the ocean are controlled by an active nitrogen cycle, whereby different chemical forms of the element are utilized as substrates for growth by a variety of microorganisms, either to supply building blocks for organic molecules, or to fuel metabolism via redox reactions (Capone et al., 2008; Kuypers et al., 2018). As a result, the residence time of fixed N in the ocean is on the order of 3,000 years or less, about one order of magnitude shorter than for the macronutrient phosphorous (Gruber and Galloway, 2008; Wang et al., 2019).
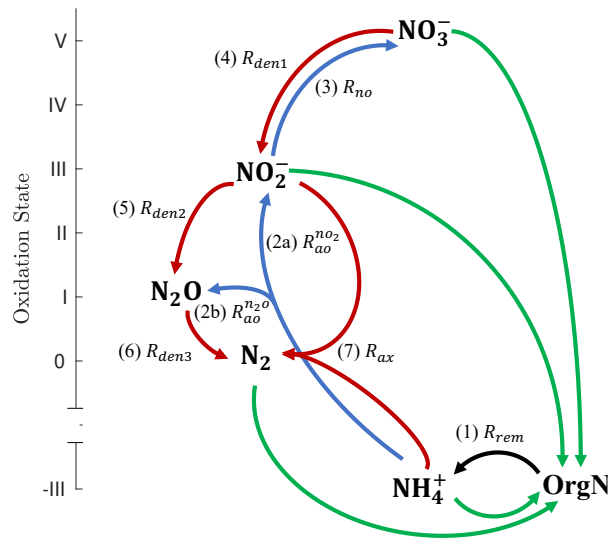
Figure 1. Schematic of the main N cycle tracers and reactions represented by NitrOMZ. Tracers are shown in bold, ordered by the oxidation state of N, and consist of organic nitrogen (OrgN), ammonium (NH_4^+), nitrate (NO_3^-), nitrite (NO_2^-), nitrous oxide (N_2O), and dinitrogen (N_2). N transformation reactions are shown as arrows connecting reactants and products. Green arrows represent nutrient uptake and nitrogen fixation rates (not explicitly represented in the model, which focuses on subsurface reactions). The black arrow corresponds to (1, R_{rem}) release of NH_4^+ by organic matter remineralization (i.e., ammonification). Blue arrows denote aerobic transformations: (2a, R_{ao}^{no2}) NH_4^+ oxidation to NO_2^-, (2b, R_{ao}^{n2o}) NH_4^+ oxidation to N_2O, and (3, R_{no}) NO_2^- oxidation to NO_3^-. Red arrows represent anaerobic processes: (4, R_{den1}) NO_3^- reduction to NO_2^-, (5, R_{den2}) NO_2^- reduction to N_2O, (6, R_{den3}) N_2O reduction to N_2, and (7, R_{ax}) anaerobic NH_4^+ oxidation (anammox) with NO_2^- to N_2.

The ocean's inventory of fixed N is dominated by NO_3^-, and the main N cycle reactions consist of uptake and assimilatory reduction of NO_3^- to NH_4^+ (here used interchangeably with ammonia, NH_3), and the oxidation of NH_4^+ back to NO_3^- following the decomposition of organic matter and nitrification (Fig. 1). Only when the concentration of dissolved oxygen (O_2) drops to suboxic or anoxic levels (typically below $5 \ \text{mmol m}^{-3}$), additional metabolic pathways involving N become

relevant, as observed in the ocean's oxygen minimum zones (OMZs) and low-O_2 sediments (Lam and Kuypers, 2011). These reactions include the three main steps of heterotrophic denitrification, i.e., the oxidation of organic carbon (OrgC) with NO_3^-, nitrite (NO_2^-), and nitrous oxide (N_2O), and anammox, the chemolithotrophic oxidation of NH_4^+ with NO_2^-. Both denitrification and anammox lead to the production of N_2, and thus remove fixed N from the ocean (Bianchi et al., 2012; DeVries et al., 2012, 2013). Ammonia oxidation is another source of N_2O — a powerful greenhouse gas and a leading agent of ozone destruction in the stratosphere. The number of N_2O molecules produced per NH_3 oxidized, i.e. the yield of this reaction, increases as O_2 declines (Goreau et al., 1980; Nevison et al., 2003) likely caused by a shift from N_2O production as a byproduct of hydroxylamine oxidation to nitrifier-denitrification (Hooper and Terry, 1979; Wrage et al., 2001; Stein and Yung, 2003). Because of denitrification and enhanced production by ammonia oxidation, OMZs are important sources of N_2O to the atmosphere (Naqvi et al., 2010; Yang et al., 2020), with the largest emissions observed right above shallow oxygen deficient waters (Arévalo-Martínez et al., 2015).

The emerging picture for the ocean's N cycle is that of a web of inter-dependent transformations that is particularly active in OMZs, where overlapping aerobic and anaerobic reactions exchange nitrogen metabolites and substrates (Lam and Kuypers, 2011; Kuypers et al., 2018), ultimately controlling fixed nitrogen removal and N_2O production. While there is evidence that organic matter and O_2 regulate the rates and relative importance of N transformations (Babbin et al., 2014; Dalsgaard et al., 2014), our mechanistic understanding of these environmental controls against the backdrop of oceanic variability remains limited. Ocean biogeochemical models can shed light on the expression of the N cycle reactions in a dynamic environment. These models have included N as a macronutrient since the beginning, representing NO_3^- and NH_4^+ assimilation by phytoplankton and subsequent nitrification (Fasham et al., 1990; Sarmiento et al., 1993; Moore et al., 2004b). With the advent of more complex Earth System Models, biogeochemical representations have progressively expanded to include more detailed representations of the N cycle, including N fixation, denitrification and N_2O production (Aumont et al., 2015; Séférian et al., 2020; Stock et al., 2020; Long et al., 2021b).

The ultimate goals of these models are multifold, and include improving predictability of oceanic N_2O emissions (Suntharalingam et al., 2012; Martinez-Rey et al., 2015; Battaglia and Joos, 2018; Buitenhuis et al., 2018; Ji et al., 2018a); providing a more realistic representation of the redox state of seawater (Louca et al., 2016); or resolving aspects of microbial dynamics underlying the oceanic N cycle (Penn et al., 2016; Zakem et al., 2018; Penn et al., 2019).

The representation of N transformations in models often relies on crude assumptions that simplify the network of N reactions and their controls to simple empirical parameterizations. For example, models that include N_2O cycling often rely on parameterizations that link N_2O production to nitrification or aerobic respiration (Suntharalingam and Sarmiento, 2000; Nevison et al., 2003; Manizza et al., 2012; Jin and Gruber, 2003), overlooking N_2O sources and sinks by denitrification. These models also conflate anammox and denitrification into a single N_2 production term. Explicit cycling of NO_2^- under low O_2, with the observed co-occurrence of NO_2^- production from NO_3^- dissimilatory reactions, reduction to N_2O and N_2 by denitrification and anammox, and reoxidation to NO_3^- are missing (Lam and Kuypers, 2011; Kalvelage et al., 2013; Babbin et al., 2014, 2015; Buchwald et al., 2015; Babbin et al., 2017).

The goal of this paper is to present a new model of the oceanic N cycle designed to be incorporated in current ocean biogeo-chemical models, with a particular focus on processes occurring within OMZs. We refer to this model as NitrOMZ (**Nitr**ogen cycling in **O**xygen **M**inimum **Z**ones). The model explicitly represents the major forms of N found in seawater as prognostic tracers, and parameterizes the transformations that connect them as a function of seawater chemistry. This formulation is informed by recent observations that describe the response of N cycle reactions to environmental controls, in particular the availability of substrates and dissolved O_2. We detail the implementation of the model in an idealized one-dimensional (1D) representation of the water column that allows comparison to in situ observations, formal optimization, and studies of the model sensitivity to parameter choices and environmental conditions.

The rest of the paper is organized as follow: Sect. 2 discusses the rationale and formulation of the model; Sect. 3 the implementation of the model; Sect. 4 the model optimization against tracer and rate observations; Sect. 5 the performance of the model and its sensitivity to environmental parameters; and Sect. 6 discusses the implications and conclusions of the work.

2 Nitrogen cycle model formulation

2.1 Model rationale

The NitrOMZ model is based on the current understanding of the N cycle in OMZs (Lam and Kuypers, 2011; Kuypers et al., 2018) as mediated by 6 major species: N_2, NO_3^-, NO_2^-, N_2O, NH_4^+ and organic nitrogen (OrgN) in either dissolved or particulate form. We only explicitly model NH_4^+ (the dominant dissolved form) and do not distinguish it from NH_3. We also assume that organic nitrogen is linked to organic carbon by fixed stoichiometry (Anderson and Sarmiento, 1994). A schematic of the model's tracers and transformation is shown in Fig. 1. Our approach represents a natural progression for current biogeochemical ocean models, and takes a "system view" of the N cycle by focusing on the biogeochemistry of N transformation reactions (Lam and Kuypers, 2011), rather than microbial ecology (Penn et al., 2016; Louca et al., 2016; Zakem et al., 2018; Penn et al., 2019). That is, the model explicitly resolves N chemical tracers and their transformations, but not the populations of microbes that are responsible for these reactions.

The underlying assumption is that the occurrence and rates of N transformations are controlled by, and can be predicted from, the physical and chemical conditions of the oceanic environment. Implicitly, the model assumes that diverse populations of microbes are always present in the water column, and that their activity (i.e., metabolic rate) is controlled by the abundance of substrates, in analogy to chemical reactions, and dissolved O_2, which inhibits anaerobic reactions (Kalvelage et al., 2011; Babbin et al., 2014; Dalsgaard et al., 2014; Ji et al., 2018a; Sun et al., 2021b). The focus on dissolved N forms and reaction rates bypasses poorly-known aspects of microbial population dynamics, which are topics of ongoing research (Louca et al., 2016; Zakem et al., 2018; Penn et al., 2019).

We assume that each reaction is implicitly mediated by specialized microorganism groups, each relying on a distinct metabolism (Lam and Kuypers, 2011; Kuypers et al., 2018). Thus, the model represents a "modular" N cycle, with individual reaction steps (i.e., individual redox reactions) represented separately, and connected by exchange of dissolved substrates (Graf et al., 2014; Kuypers et al., 2018). This premise is grounded on observations of high specialization and streamlined genomes for marine prokaryotes (Giovannoni et al., 2014), including microorganisms carrying genes for N-based metabolic reactions (Ganesh et al., 2015; Kuypers et al., 2018).

These assumptions are sufficient to provide a broad representation of microbial N transformations and their environmental expressions in the ocean, while limiting model complexity and the proliferation of poorly-constrained parameters. They are also grounding steps towards models that explicitly represent microbial populations, including their diversity and dynamics in OMZs (Louca et al., 2016; Penn et al., 2016; Zakem et al., 2018; Penn et al., 2019).

2.2 Model tracers and processes

The model focuses on microbial processes that take place below the euphotic zone, as driven by the flux of organic matter produced near the surface and exported into the ocean interior by the biological pump (Boyd et al., 2019). We include heterotrophic and chemolithotrophic pathways that are commonly observed in the open ocean and require N species as substrates

(Kuypers et al., 2018) (Fig. 1). Additional pathways, for example involving sulfur or iron, could also be represented following a similar approach.

Heterotrophic reactions resolved by the model (Fig. 1) consist of aerobic organic matter respiration (R_{rem}, pathway 1), which relies on O_2 as the oxidant, and the three main steps of denitrification: dissimilatory NO_3^- reduction to NO_2^- (R_{den1}, pathway 4), NO_2^- reduction to N_2O (R_{den2}, pathway 5), and N_2O reduction to N_2 (R_{den3}, pathway 6). Chemolithotrophic processes consist of aerobic oxidation of NH_4^+ to both NO_2^- (R_{ao}^{no2}, pathway 2a) and N_2O (R_{ao}^{n2o}, pathway 2b via both hydroxylamine oxidation and nitrifier-denitrification), aerobic oxidation of NO_2^- to NO_3^- (R_{no}, pathway 3), and anammox, the anaerobic oxidation of NH_4^+ with NO_2^- to produce N_2 gas (R_{ax}, pathway 7). Reactions are parameterized as functions of substrates (i.e., model tracer concentrations) and environmental parameters such as dissolved O_2 and organic matter. Tracers are expressed as concentrations, with units of $mmol\,m^{-3}$.

We do not include an explicit representation of nitric oxide, NO, because of the poor understanding of its cycle in the marine environment (Ward and Zafiriou, 1988). NO is thought to be an obligate intermediate or a byproduct of N cycle reactions, including nitrification and denitrification (Schreiber et al., 2012). However, it is a very reactive chemical with extremely low concentrations (on the order of $pmol\,m^{-3}$) and rapid turnover in seawater (Ward and Zafiriou, 1988). As a consequence, in situ NO observations are limited (Lutterbeck et al., 2018), and rate measurements targeting NO reactions are missing. Impicitly, we assume that NO cycles so rapidly that accumulation and transport by the oceanic circulation are negligible, and that its dynamics can be folded into the cycle of other N tracers.

There are also several notable processes that are not represented in the current model formulation, but could be introduced in future releases. Some of these processes (e.g., dissimilatory NO_2^- reduction to NH_4^+, DNRA) are not thought to be quantitatively relevant in oceanic oxygen minimum zones. Others, while relevant, require further measurements to constrain their significance and response to environmental variability.

Production of N_2O via NH_4^+ oxidation in NitrOMZ is represented as a single O_2-dependent function designed to model the transition in bacterial metabolisms from predominantly hydroxylamine oxidation to nitrifier-denitrification at low O_2 (Hooper and Terry, 1979; Wrage et al., 2001; Stein and Yung, 2003; Nevison et al., 2003). However, growing evidence suggests that ammonia oxidizing archaea (AOA, which greatly outnumber their bacterial counterparts) can also produce N_2O via a hybrid mechanism (Santoro et al., 2011; Löscher et al., 2012). Production of N_2O via AOA appears to be similarly enhanced at low O_2 (Trimmer et al., 2016; Santoro et al., 2021), although evidence from Stieglmeier et al. (2014) argues otherwise.

DNRA, which can be dominant in anoxic sediment, has been sporadically observed in the water column of oxygen deficient zones, where it may provide an additional source of NH_4^+ to anammox bacteria (Lam et al., 2009; Lam and Kuypers, 2011; Kraft et al., 2011; Jensen et al., 2011). However, DNRA is commonly undetectable in OMZ waters (Kalvelage et al., 2013; De Brabandere et al., 2014) , and its importance to the N cycle of OMZ is still debated (Long et al., 2021a).

Recent tracer incubation studies show substantial and often dominant formation of N_2O from NO_3^- rather than NO_2^- (Ji et al., 2018b; Frey et al., 2020). This suggests that denitrifying bacteria capable of direct production of N_2O from NO_3^- reduction (as NO_2^- reduction proceeds entirely within the cell) could be a major source of N_2O. This idea, which contrasts with the model assumption of a fully "modular"' N cycle, is further supported by isotopic evidence (Casciotti et al., 2018).

Observations needed to constrain the proportion of N_2O from NO_3^- and NO_2^- and its environmental sensitivity remain however limited (Ji et al., 2018b; Frey et al., 2020).

Finally, the model could easily accommodate missing processes that couple the N cycle with other elemental cycles, in particular carbon and sulfur. These include formation of organic matter by chemolithotrophy, changes in inorganic carbon chemistry (e.g., pH) by anaerobic reactions (Cinay et al., 2022) , and additional metabolic pathways such as anaerobic oxidation of sulfide with NO_3^- (Callbeck et al., 2021), and anaerobic oxidation of methane with NO_2^- (Thamdrup et al., 2019), both chemolithotrophic denitrification reactions.

2.3   Model equations

Heterotrophic reactions (i.e., organic matter remineralization) are parameterized as a function of the respective oxidants and organic matter concentration, and expressed in carbon units per unit volume and time. Heterotropic reaction rates are assumed to be first-order in the concentration of organic matter, and limited by the oxidant following a Michelis-Menten formulation (Johnson and Goody, 2011). Anaerobic reactions are inhibited by the presence of O_2, based on an exponential limitation term (Dalsgaard et al., 2014). The resulting equation for a general heterotropic reaction is:

$$R_H = k_H \cdot \frac{[X]}{[X] + K_H^X} \cdot e^{-\frac{O_2}{K_H^{o2}}} \cdot \text{POC} \tag{1}$$

Here, H indicates the heterotrophic process considered (e.g., dissimilatory reduction of NO_3^- to NO_2^-), R_H the heterotrophic reaction rate (mmol C m^{-3} s^{-1}); k_H the specific first-order reaction rate (s^{-1}); $[X]$ the concentration of the oxidant (i.e., O_2, NO_3^-, NO_2^- or N_2O); K_H^X the half saturation constant for oxidant uptake (mmol m^{-3}); K_H^{o2} the scale for inhibition of the reaction by O_2 (mmol m^{-3}); and POC the concentration of particulate organic matter in units of mmol C m^{-3}. No O_2 inhibition is applied to aerobic respiration (i.e., K_H^{o2} can be thought of as arbitrarily large).

Chemolithotropic reactions are proportional to the respective substrates. A maximum reaction rate is modulated by the concentration of oxidants and reductants, following Michelis-Menten dynamics. For anaerobic reactions (here, anammox), an O_2-dependent inhibition term limits the reactions when O_2 is present. The resulting equation for a general chemolithotrophic reaction is:

$$R_A = k_A \cdot \frac{[X]}{[X] + K_A^X} \cdot \frac{[Y]}{[Y] + K_A^Y} \cdot e^{-\frac{O_2}{K_A^{o2}}}. \tag{2}$$

Here, A indicates the chemolithotropic process considered (e.g. anammox), R_A the reaction rate (mmol N m^{-3} s^{-1}); k_A the maximum reaction rate when the process is not limited (mmol N m^{-3} s^{-1}); $[X]$ and $[Y]$ the concentrations of the oxidant and reductant respectively (e.g., NO_2^- and NH_4^+ for anammox); K_A^X and K_A^Y the half saturation constants for oxidant and reductant uptake respectively (mmol m^{-3}); and K_A^{o2} the scale for inhibition of the reaction by O_2 (mmol m^{-3}). For aerobic reactions, K_A^{o2} is set to infinite, removing O_2 inhibition.

Equations for each of the heterotrophic and chemolithotrophic reactions are presented in Appendix A1 and A2, respectively; parameter names, units, and suggested values from the literature are presented in Table 1.

2.4 Model assumptions and parameterizations

In the model, we assume that heterotropic reactions are first-order to the concentration of organic matter, thus all organic matter can be utilized by microorganisms without saturation at high concentrations. Because of the low abundance of organic matter in seawater, and extensive colonization of particles by heterotrophic bacteria, this is a reasonable first-order assumption. However, see Nguyen et al. (2022) for a discussion of microbial-particle interactions in ocean biogeochemical models, and more complex aspect of their dynamics. For simplicity, we represent organic carbon by a single component. This assumption is easily relaxed to include multiple carbon species, for example separate particulate or dissolved forms.

We do not explicitly model conversion of dissolved CO_2 to organic matter by chemolithotrophy, because of the small rates compared to the remineralization of organic matter in the upper ocean. This assumption can also be relaxed in future implementations of the model, allowing a more complete integration between chemolithotrophy and the carbon cycle.

The use of an exponential inhibition term for anaerobic reactions by O_2 is based on the observation that they are limited at O_2 concentrations of few $\mathrm{mmol\,m^{-3}}$ or smaller (Dalsgaard et al., 2014; Babbin et al., 2015; Frey et al., 2020). However, coexistence of anaerobic and aerobic reactions at O_2 concentrations of 10–20 $\mathrm{mmol\,m^{-3}}$ or higher is also observed (Kalvelage et al., 2011), perhaps related to the presence of redox microenvironments within organic particles (Bianchi et al., 2018; Smriga et al., 2021), which are not explictly considered here. The exponential inhibition formulation has the advantage of being controlled by a single parameter, allows anaerobic reactions at finite O_2 concentrations, and approximates empirical rates from incubation experiments reasonably well (Dalsgaard et al., 2014).

Parameter values for maximum reaction rates, half saturation constants, and O_2 inhibition terms (Eq. (1) and (2)), are informed by analysis of previous work, and further optimized against in situ observations of tracers and rates (Sect. 4). Table 1 presents a list of the model parameters and measured values based on a review of the literature. Note that these studies are based on shipboard and laboratory incubations that differ in the setup, conditions, and microbial populations tested. Despite these caveats, experimental results provide valuable starting points to further constrain parameter values in the model.

Table 1. Summary of the main NitrOMZ parameters, with any reported values from the literature (not available or 'N/A' otherwise).

Parameter	Description	Units	Value(s)	Source(s)
k_{rem}	Maximum aerobic remineralization rate	d^{-1}	0.08	Babbin et al. (2015)
k_{ao}	Maximum NH_4^+ oxidation rate	$\mu mol\ N\ m^{-3}\ d^{-1}$	45.56 ± 4.8	Bristow et al. (2016)
			37.10 ± 1.2	Peng et al. (2016)
			20 - 100	Ward (2008)
k_{no}	Maximum NO_2^- oxidation rate	$\mu mol\ N\ m^{-3}\ d^{-1}$	255.5 ± 17.3	Bristow et al. (2016)
			63.3 ± 13.8	Sun et al. (2017)
			55.7 ± 5.4	Sun et al. (2017)
k_{den1}	Maximum NO_3^- reduction rate	$\mu mol\ N\ m^{-3}\ d^{-1}$	197 ± 26	Bristow et al. (2016)
k_{den2}	Maximum NO_2^- reduction rate	$\mu mol\ N\ m^{-3}\ d^{-1}$	N/A	N/A
k_{den3}	Maximum N_2O reduction rate	$\mu mol\ N\ m^{-3}\ d^{-1}$	N/A	N/A
k_{ax}	Maximum anammox rate	$\mu mol\ N\ m^{-3}\ d^{-1}$	N/A	N/A
K_{rem}^{o2}	O_2 half saturation constant for oxic remineralization	$mmol\ O_2\ m^{-3}$	4	Babbin et al. (2015)
K_{ao}^{nh4}	NH_4^+ half saturation constant for NH_4^+ oxidation	$mmol\ N\ m^{-3}$	0.134 ± 0.005	Martens-Habbena et al. (2009)
K_{ao}^{o2}	O_2 half saturation constant for NH_4^+ oxidation	$mmol\ O_2\ m^{-3}$	0.33 ± 0.13	Bristow et al. (2016)
			3.6 ± 0.6	Peng et al. (2016)
K_{no}^{no2}	NO_2^- half saturation constant for NO_2^- oxidation	$mmol\ N\ m^{-3}$	0.254 ± 0.161	Sun et al. (2017)
K_{no}^{o2}	O_2 half saturation constant for NO_2^- oxidation	$mmol\ O_2\ m^{-3}$	0.778 ± 0.168	Bristow et al. (2016)
K_{den1}^{no3}	NO_3^- half saturation constant for NO_3^- reduction	$mmol\ N\ m^{-3}$	N/A	N/A
K_{den2}^{no2}	NO_2^- half saturation constant for NO_2^- reduction	$mmol\ N\ m^{-3}$	N/A	N/A
K_{den3}^{n2o}	N_2O half saturation constant for N_2O reduction	$mmol\ N\ m^{-3}$	N/A	N/A
K_{ax}^{nh4}	NH_4^+ half saturation constant for anammox	$mmol\ N\ m^{-3}$	N/A	N/A
K_{ax}^{no2}	NO_2^- half saturation constant for anammox	$mmol\ N\ m^{-3}$	N/A	N/A
K_{den1}^{o2}	O_2 exponential inhibition for NO_3^- reduction	$mmol\ O_2\ m^{-3}$	1.05 ± 0.72	Bristow et al. (2016)
K_{den2}^{o2}	O_2 exponential inhibition for NO_2^- reduction	$mmol\ O_2\ m^{-3}$	0.429 ± 0.2	Dalsgaard et al. (2014)
			2.16 ± 1.3	Ji et al. (2018a)
K_{den3}^{o2}	O_2 exponential inhibition for N_2O reduction	$mmol\ O_2\ m^{-3}$	0.27 ± 0.05	Dalsgaard et al. (2014)
K_{ax}^{o2}	O_2 exponential inhibition for anammox	$mmol\ O_2\ m^{-3}$	1.28 ± 0.6	Dalsgaard et al. (2014)
Ji_a	Nevison et al. (2003) 'a' parameter	%	0.11 ± 0.05	Santoro et al. (2021)
			0.2 ± 0.13	Ji et al. (2018a)
Ji_b	Nevison et al. (2003) 'b' parameter	%	0.077 ± 0.07	Santoro et al. (2021)
			0.08 ± 0.04	Ji et al. (2018a)

3 Model implementation

3.1 One-dimensional model setup

We implement the model for a 1D water column that includes physical transport by vertical advection and turbulent diffusion (Wyrtki, 1962), and, if required, parameterized lateral transport by horizontal currents and eddies (Gnanadesikan et al., 2013; Bettencourt et al., 2015). The model is configured to represent the typical weak upwelling conditions that characterize open-ocean oxygen minimum zones, following previous work (Babbin et al., 2015).

In the 1D framework, the conservation equation for the concentration [C] of a generic dissolved tracer can be written as:

$$\frac{\partial [\mathrm{C}]}{\partial t} = -\frac{\partial \left(w_u \cdot [\mathrm{C}]\right)}{\partial z} + \frac{\partial}{\partial z} K_v \frac{\left(\partial [\mathrm{C}]\right)}{\partial z} + \sum_{i=1}^{N_H} \left(r_{C,H}^i \cdot R_H^i\right) + \sum_{i=1}^{N_A} \left(r_{C,A}^i \cdot R_A^i\right) + LT \tag{3}$$

Here, w_u is the vertical upwelling velocity ($\mathrm{m\,s^{-1}}$) and K_v is the vertical turbulent diffusion coefficient ($\mathrm{m^2\,s^{-1}}$, distinct from molecular diffusion which is much smaller), both of which can be a function of depth. The first and second summation are respectively over the N_H heterotrophic and N_A chemolithotrophic processes that involve the tracer (Eq. (1) and (2)), with $r_{C,H}^i$ and $r_{C,A}^i$ the corresponding stoichiometric ratios (Appendix A4). LT represents any parameterized lateral transport process. The explicit equations for each of the model tracers are detailed in Appendix A5.

The lateral transport terms LT can be included to parameterize horizontal circulation by advection and diffusion in the 1D framework. Typically, these terms are simplified by a linear restoring to far-field tracer concentration profiles (Babbin et al., 2015), $[\mathrm{C}]^{far}$, with a relaxation timescale τ_C (s):

$$LT = -\frac{1}{\tau_C} \cdot \left([\mathrm{C}] - [\mathrm{C}]^{far}\right) \tag{4}$$

For typical open ocean conditions, τ_C can be estimated as the minimum of an advective timescale $\frac{L}{U}$ and a diffusive timescale, $\frac{L^2}{K_H}$, where L, U, K_H are respectively the horizontal spatial scale, the horizontal velocity scale, and the horizontal eddy diffusion. Assuming L on the order of 1000 km, U on the order of 0.01 $\mathrm{m\,s^{-1}}$, and K_H on the order of 1000 $\mathrm{m^2\,s^{-1}}$ results in a timescale $\tau_C = 10^8$ s, i.e., on the order of 3 years and in agreement with recent estimates of the residence time of water within the Eastern Tropical South Pacific (ETSP) (Ji et al., 2015b; Johnston et al., 2014).

3.2 Organic matter remineralization

In the 1D model implementation, we represent organic matter (OrgC and OrgN) as a single particulate organic carbon (POC) class that sinks through the water column. We assume that this sinking is rapid compared to advection and diffusion, leading to a steady-state distribution of POC that is only controlled by sinking and remineralization (Kriest and Oschlies, 2008). Since remineralization rates are proportional to the concentration of organic matter, the resulting steady-state 1D equation for POC is:

$$\frac{\partial \left(w_s \cdot \mathrm{POC}\right)}{\partial z} = -\sum_{i=1}^{N_H} R_H^i = \sum_{i=1}^{N_H} \left(k_H^{eff,i}\right) \cdot \mathrm{POC} \tag{5}$$

Here, w_s is the depth-dependent sinking speed of POC in the water column, and $k_H^{eff,i}$ (s^{-1}) are the effective rate constants for each heterotrophic process, i.e., the maximum rate constants multiplied by the respective substrate limitation and O_2 inhibition terms (Eq. (1)).

Considering the flux of sinking POC, Φ_{POC} ($mmol\,C\,m^{-2}\,s^{-1}$):

$$\Phi_{POC} = w_s \cdot POC, \tag{6}$$

equation 5 can be written as:

$$\frac{\partial \Phi_{POC}}{\partial z} = -\sum_{i=1}^{N_H} R_H^i = -\sum_{i=1}^{N_H} \left(k_H^{eff,i} \right) \cdot POC, \tag{7}$$

or, equivalently,

$$\frac{\partial \Phi_{POC}}{\partial z} = -\frac{\sum_{i=1}^{N_H} \left(k_H^{eff,i} \right)}{w_s} \cdot \Phi_{POC} \tag{8}$$

Equation 7 can be recast to relate the concentration of POC in the water column to the remineralization of the POC flux with depth:

$$POC = -\frac{1}{\sum_{i=1}^{N_H} \left(k_H^{eff,i} \right)} \cdot \frac{\partial \Phi_{POC}}{\partial z} \tag{9}$$

The advantage of Equation 9 is that it allows to diagnose sinking POC concentrations when the POC flux and remineralization rate constants are known. In the 1D implementation of the model, we parameterize the POC flux following a typical depth-dependent power-law function, or Martin curve (Martin et al., 1987; Berelson, 2001; Primeau, 2006):

$$\Phi_{POC} = \Phi_{POC}(z_0) \cdot \left(\frac{z}{z_0} \right)^{-b}, \tag{10}$$

where z_0 is the upper boundary of the model, and b the power-law or Martin coefficient. A plot of the model POC is shown in Fig. C1. Another advantage of this formulation is that it allows coupling NitrOMZ to more complex parameterizations for the remineralization of organic matter in ocean biogeochemical models, some of which rely on explicit representation of sinking organic particles, and some of which only represent sinking organic particle fluxes in the water column (Moore et al., 2004a; Dunne et al., 2010; Aumont et al., 2015; Stock et al., 2020; Long et al., 2021b). Because NitrOMZ's equation can be cast as a function of prescribed vertical organic matter flux or remineralization profiles, the model can be coupled to existing biogeochemical models with minimal interference with their formulation of organic matter cycles.

3.3 Numerical implementation of the 1D model

For the purpose of testing and illustration, we implement NitrOMZ in a 1D representation of the water column below the mixed layer, following previous work (Babbin et al., 2015). Model tracers are discretized on a 1D vertical grid, with equal spacing $\Delta z = 10\,m$, where z is depth. Boundary conditions are set at the top (z_0) and bottom grid (z_{bot}) cells, as Dirichlet (or

fixed concentration) boundary conditions, with values taken from observations (Tables B2 - B3). The conservation equation for each tracer (following Eq. (3), see Appendix A5 for full equations) is then solved using a forward in time, centered in space numerical scheme, with a constant vertical grid spacing, and the option for a variable or constant timestep. In the baseline simulations (Fig. 2), we adopt a timestep of 5 days for the initial 650 year spinup, and decrease it to 3 hours for the final two years of the simulation (years 698 and 699) to increase accuracy.

As in Babbin et al. (2015), NitrOMZ does not represent primary production in the surface layer, and is instead forced at the uppermost boundary by a flux of sinking POC, $\Phi_{POC}(z_0) = w_s(z_0) \cdot POC(z_0)$, where $POC(z_0)$ provides the boundary condition for POC. The flux Φ_{POC} remineralizes in the water column based on a Martin curve profile (Eq. (10)). At each depth, the steady-state conservation equation for POC (Eq. (8)) is solved with a forward-in-space method, using a depth-dependent sinking speed w_s chosen to produce, together with the maximum aerobic remineralization rate constant, k_{rem}, a POC flux profile matching a Martin curve with exponent b appropriate for the oxygenated ocean (Primeau, 2006; Weber and Bianchi, 2020). To this end, the sinking speed is calculated at each depth as:

$$w_s = \frac{k_{Rem} \cdot z}{b} \tag{11}$$

The concentration of POC in the water column is then diagnosed using Equation 9, and used to calculate the heterotrophic remineralization rates R_H in Equation 1 (see Appendix A1).

Under constant forcings and boundary conditions, the model tracers evolve towards steady-state ($\frac{\partial [C]}{\partial t} \approx 0$, Fig. 2) with a timescale τ_{SS} that can be estimated from the advection velocity w_u, the turbulent vertical diffusion K_v, and the vertical scale H, as the minimum between $\frac{H}{w_u}$ and $\frac{H^2}{K_v}$. For w_u on the order of 10 m y^{-1}, K_v on the order of 10^{-5} m^2 s^{-1}, and a vertical scale of 1000 m, the timescale to approach steady-state is $\tau_{SS} = 3 \cdot 10^{10}$ s, or about 100 years.

Fig. 2 shows an example of model spinup to steady state in NitrOMZ, with parameters taken from an optimal solution discussed in Sect. 5.2, and uniform initial tracer concentrations in the water column. At the start of the simulation, high water column O_2 leads the aerobic remineralization (R_{rem}) to dominate total POC consumption. As the simulation proceeds, an O_2 minimum develops in subsurface waters, reaching suboxic (< 10 mmol O_2) concentrations around year 100. NO_3^- reduction rates (R_{den1}) are relieved of O_2 inhibition and begin to take up a larger fraction of total POC remineralization, as revealed by the depletion of N*, signaling NO_3^- consumption in the water column. Reduction of NO_3^- also leads to a subsurface peak in NO_2^- within the O_2-minimum (Fig. 2). With newly available NO_2^- substrate and low O_2 conditions, NO_2^- reduction (R_{den2}) begins, resulting first in a subsurface spike in N_2O. With further decrease in O_2 concentrations, N_2O is reduced to N_2, leading to a layer of low N_2O concentrations within the OMZ that persists to the end of the simulation. Anammox (R_{ax}) is similarly relieved of O_2 inhibition as the O_2-minimum is established, reaching maximum values near the upper oxycline, reflecting relatively high supply of both NO_2^- and NH_4^+.
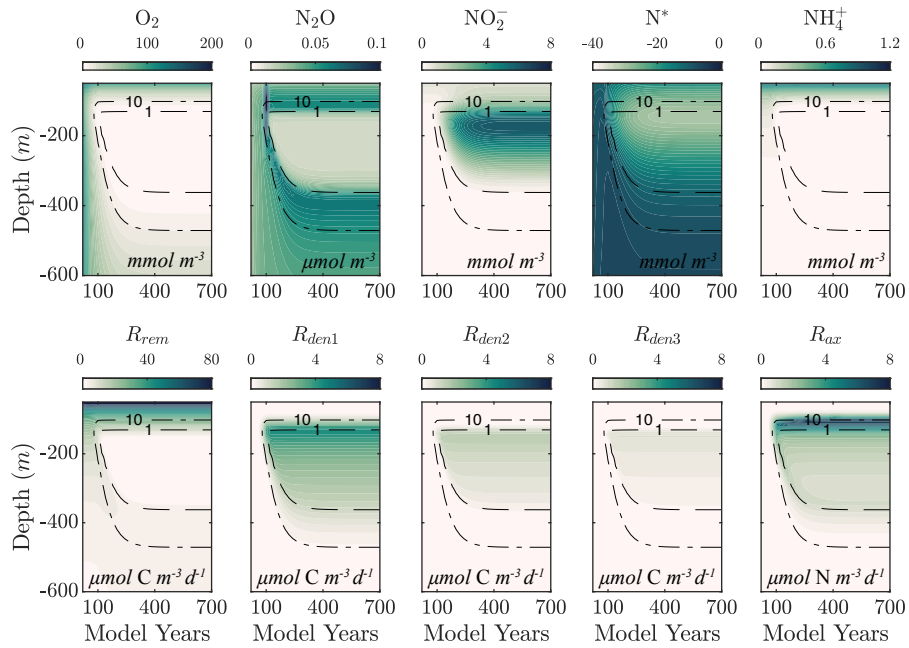
Figure 2. Example of spinup of the model. (top) Temporal evolution of O_2, N_2O, NO_2^-, N^*, and NH_4^+ from initial ETSP boundary conditions at year 0 to the final model solution at year 700 using the selected parameter set (Opt_{sel}) discussed in Sect. 5.2. Dashed black curves highlight the 1 and 10 mmol O_2 m^{-3} contours. (bottom) Same as (top), but for the heterotrophic rates of aerobic respiration (R_{rem}), NO_3^- reduction (R_{den1}), NO_2^- reduction (R_{den2}), and N_2O reduction (R_{den3}). The chemolithotrophic anammox rate (R_{ax}) is also shown in the far right panel.

4 Model optimization strategy

The model contains 23 major parameters that control the N cycle, some of which are relatively well constrained by observations, whereas others are poorly known and can plausibly span a broad range of values (Table 1). In the model, these parameters approximate complex or poorly known aspects of microbial physiology, metabolism and ecology, and thus are intrinsically uncertain. In order to select a set of parameters that produces a realistic representation of the N cycle in OMZ, we adopt a "metaheuristic" approach based on application of an optimization algorithm, following an established strategy in ocean biogeochemistry (Schartau and Oschlies, 2003; Ward et al., 2010; Kriest et al., 2017).

To conduct this optimization, we compile available tracer and biogeochemical rate observations for the ETSP OMZ from a July 2013 cruise aboard the R/V Nathaniel B. Palmer, for which abundant trace and rate measurements are available (Fig. 5) (Ji et al., 2015b; Peng et al., 2016; Babbin et al., 2017, 2020), as well as from other cruises in the region (Kalvelage et al., 2013). The observations are then used to define a cost function based on normalized squared deviations between model profiles and observations. The cost function is minimized by applying a Covariance Matrix Adaptation Evolutionary Strategy algorithm (CMA-ES, discussed in Section 4.1), which finds a local optimal solution in the model's multi-dimensional parameter landscape.

The optimization is characterized by large dimensionality, strong non-linearity, a significant computational cost (requiring several 10,000s model runs to converge), and inherent flexibility in the formulation of the cost function (Schartau and Oschlies, 2003; Kriest et al., 2017). Thus, instead of seeking a single global optimal solution, we generate an ensemble of optimal solutions that provide equally acceptable representations of OMZ processes based on the cost function. To this end, we apply the optimization multiple times, varying the formulation of the cost function slightly, and assigning a random error to the observations for each optimization (Table B4). As a result, we produce a set of equally plausible optimal solutions that we further evaluate to select a final parameter set based on additional comparisons with observations, which we use for further analysis.

4.1 Optimization algorithm

The CMA-ES is a stochastic, population-based algorithm that seeks to minimize an objective cost function (Hansen et al., 2009). The CMA-ES falls within the broader class of evolutionary optimization algorithms, where search for an optimal solution proceeds by an iterative improvement of a population of parameters, with each iteration including a stochastic "evolutionary" element, in loose analogy with biological processes of mutation, recombination, and selection (illustrated in Fig. 3). In contrast with typical evolutionary computation algorithms such as Genetic Algorithms, in the CMA-ES the mutation and recombination operations are substituted by sampling from a multivariate normal distribution in which parameters (the covariance matrix) are deterministically updated based on previous iteration steps (Hansen, 2006).

The CMA-ES has been shown to be more efficient (i.e., requiring fewer objective function evaluations), accurate (i.e., able to approximate the global optimum when it is known to exist), and robust (i.e., not overly sensitive to the initial choice of parameters), compared to other optimization algorithms, when applied to multi-dimensional, non-linear optimization problems

(Hansen et al., 2009; Hansen, 2023). These properties make it suitable for optimization of ocean biogeochemical models (Kriest et al., 2017). A detailed description of the algorithm procedure can be found in Hansen (2023); an overview of the main steps of the algorithm, and its application to ocean biogeochmsitry are presented in Kriest et al. (2017).
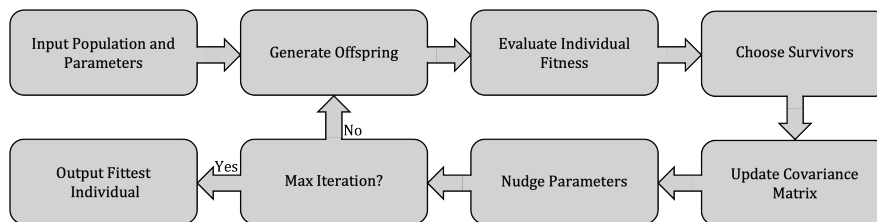
Figure 3. Flowchart of the CMA-ES optimization algorithm used to constrain uncertain model parameters.

4.2 Optimization implementation

As an illustration of NitrOMZ, we perform a series of optimizations against ETSP OMZ observations. For this configuration, we set a constant upwelling velocity (w_{up}) but impose a variable vertical diffusion (K_v) profile, with lower diffusion in upper stratified layers, and a transition to higher diffusion in deeper layers (Fischer et al., 2013) (Fig. C1, left panel). This is a simplifying assumption that allows us to control the vertical scale for advective-diffusive transport (given by the ratio between vertical diffusivity and upwelling velocity, $\frac{K_v}{w_{up}}$), without requiring vertical divergence terms in the conservation equation for tracers associated with variable vertical velocities. Since this simulation targets the core of the OMZ, generally characterized by sluggish horizontal circulation (Karstensen et al., 2008), we turn off far-field tracer restoring. This simplifies analysis of model balances between transport and reaction rates, while resulting in realistic tracer distributions. Top and bottom boundary conditions are listed in Table B3 and are extracted from observations.

As a first step, we select parameters that control aerobic remineralization processes (R_{rem}) and lead to a realistic vertical O_2 profile relative to ETSP observations, including the vertical position and thickness of oxygen deficient waters ($O_2 < 5$ mmol m^{-3}) (Fig. 5). These consist of the vertical diffusion and upwelling magnitude, the Martin curve coefficient (b), and the upper ocean POC flux (Φ_{poc}^{top}), based on values consistent with observations (Table B2 and Fig. C1). For simplicity, we also set the maximum aerobic remineralization rate (k_{rem}) and the O_2 half saturation constants for NH_4^+ and NO_2^- oxidation ($K_{ao}^{o_2}$ and $K_{no}^{o_2}$, respectively) to reported values in the literature (see Table 1). We then employ the CMA-ES algorithm in NitrOMZ to optimize the remaining 20 parameters that control heterotrophic and chemolithotrophic reactions in Fig. 1, using the range of parameter values listed in Table B1.

To optimize more uncertain parameters that control the anaerobic N cycle, we then conduct 4 sets of optimizations, with cost functions devised to match desired characteristics of tracer and rate profiles in the ETSP OMZ. Briefly, the cost function is calculated as the mean square of the difference between observations and model output profiles for a series of variables that include tracers and N transformation rates (listed in Table B4). Before each optimization, a random error of 20% is assigned

to each observation to increase the variability of observational constraints and improve the robustness of the optimization

340   ensemble by preventing from always converging in the neighborhood of a specific local minimum controlled by non-relevant features of the observations. Three additional constraints are imposed to improve the fit to observations for N cycle processes occurring within the core of the OMZ. First, all rates are weighted equally, whereas different weights are assigned to each tracer, giving higher weight to N_2O and NO_2^-, which are central to the anaerobic N cycle. Because of possible influence from horizontal advection in observations, discrepencies exist between modelled and observed NO_3^- and PO_4^{3-}. To compensate for

345   this, we also assign lower weights to NO_3^- and PO_4^{3-}, and higher weight to N^*. Second, a depth-dependent weighting scheme is included to emphasize the match to observations in the OMZ interior. This vertical weight is shaped as a Gaussian curve centered at the core of the observed OMZ, where the bulk of anaerobic transformations targeted by our model occurs, so that values within the core of the OMZ are weighted up to twice as much as values outside the OMZ. Finally, N cycle transformation rates are shifted vertically to match their depth relative to the oxycline (here defined as O_2=1 mmol m^{-3}) in both model and

350   observations, and rescaled by a factor proportional to observed vs. modeled POC flux in the upper ocean. The only difference between the 4 sets of optimization are the relative weights assigned to each tracer, listed in Table B4. In total, we obtain 382 optimized parameter sets for further analysis.

5 Results and sensitivity

5.1 Optimization results

The distributions of the parameter values from the 382 sets of optimizations (see Sect. 4.2 and Table B4) are shown in Fig. C2. Rather than converging always to the same set of parameters, the optimization shows some variability for specific parameters. This reflects the stochastic nature of the CMA-ES algorithm, the inclusion of random variations in the observations, and the highly non-linear nature of the optimization problem, which may allow for non-unique optimal solutions. Optimized maximum rates (such as k_{ao}, k_{no}, k_{den1}, and k_{den3}) and exponential O_2 inhibition parameters for step-wise denitrification ($K_{den2}^{o_2}$ and $K_{den3}^{o_2}$) reveal more variability than half-saturation concentration coefficients (K terms), which often settle to the minimum or maximum allowed value (Table B1).

Pairwise correlations in Fig. 4 reveal several parameters pairs which exhibit strong relationships, reflecting the fact that, in a significantly non-linear optimization, similar results can be obtained by trade-offs between different parameters and processes. Notably, the exponential O_2 inhibition constants for NO_2^- and N_2O reduction ($K_{den2}^{o_2}$ and $K_{den3}^{o_2}$, respectively) are strongly correlated with each other (R = 0.73) and with other parameters controlling the denitrification steps. These include positive correlations with the maximum rate parameters for NO_3^- and NO_2^- reduction (k_{den1} and k_{den2}, respectively) and negative correlations with the half-saturation constants for NO_2^- and N_2O reduction (K_{den2}^{no2} and K_{den3}^{n2o}, respectively). These correlations suggests tight couplings between modelled denitrification steps, wherein high/low maximum denitrification rates can be compensated by lower/higher half-saturation coefficients, respectively.
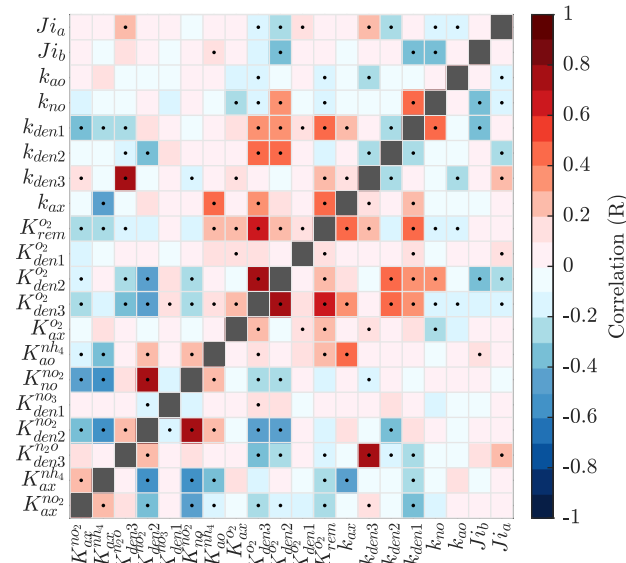
Figure 4. Pairwise correlations between model parameters for model solutions optimized for the ETSP OMZ. See Table B1 for a list and a description of the model parameters. Correlation is shown as the Pearson correlation coefficient, with dots representing p-values < 0.01.

370 Considering the variability in the optimal parameter sets, and the complexity of the cost function, which depends on observations for multiple variables at different depths, the resulting N-cycle profiles show similar features across all optimal solutions (Fig. 5, top panels; see also Fig. C3 for macronutrient profiles). When compared to observations, the majority of parameter sets are able to skillfully model (1) the vertical distribution of O_2, including the oxygen deficient layer between roughly 100 to 400 m, (2) the subsurface maximum in NO_2^-, (3) the rapid attenuation of NH_4^+ with depth, and (4) the subsurface minimum in N^*.

375 N cycle transformation rates also show similar consistency in their vertical profiles, albeit with more notable discrepancies with observations, possibly reflecting the higher variability and more complex nature of these measurements. Lower rates than observed may also reflect the fact that incubation experiments provide potential rates, rather than in situ rates. In general, the yield of N_2O from NH_4^+ oxidation (R_{ao}^{n2o}) is $\mathcal{O}(100)$ times less than for NO_2^- (R_{ao}^{no2}) following Equations A8 and A9, consistent with observations (Ji et al., 2015a, 2018a; Santoro et al., 2021). The step-wise denitrification rates (R_{den1}, R_{den2}, and

380 R_{den3}) show remarkably similar vertical profiles, with higher NO_3^- reduction rates (R_{den1}) and nearly identical magnitudes between R_{den2} and R_{den3}. Anammox (R_{ax}) shows a similar profile as denitrification, albeit with enhanced local maxima near the upper and lower oxycline depths surrounding the OMZ core, consistent with observations (Kalvelage et al., 2013).
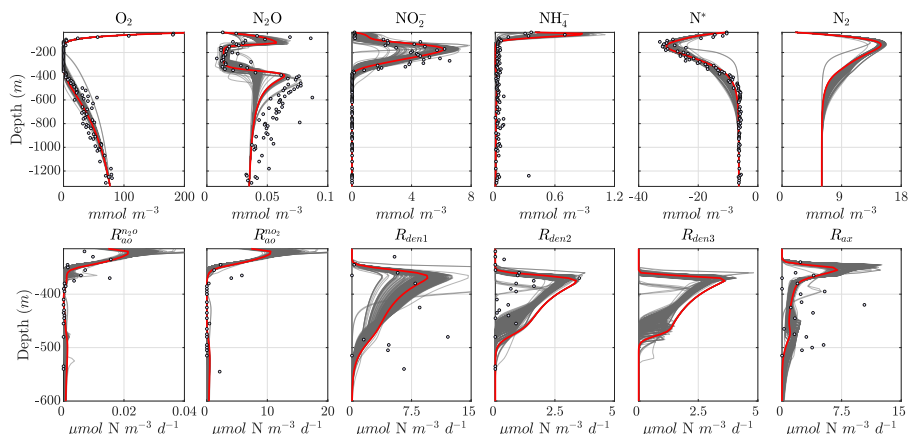
Figure 5. Results from the optimized ensemble of model solutions. (top) Tracer (O_2, N_2O, NO_2^-, NH_4^+, N^*, and N_2) profiles from all 382 optimized ETSP parameter sets. The bold red curves show the selected parameter set (Opt_{sel}) discussed in Sect. 5.2. Observations used to define the optimization cost function are shown as circles in each panel. Macronutrient profiles (NO_3^- and PO_4^{3-}) are shown in Fig. C3. (bottom) Same as in (top), but for reaction rate profiles of N_2O and NO_2^- production from NH_4^+ oxidation (R_{ao}^{n2o} and R_{ao}^{no2}, respectively), NO_3^- NO_2^-, and N_2O reduction (R_{den1}, R_{den2}, and R_{den3}, respectively) and anammox (R_{ax}).

Several robust features emerge from the optimized parameter solutions, suggesting underlying mechanisms that need to be captured for a faithful representation of the OMZ N cycle. In particular, the differences in the exponential O_2 inhibition

385 parameters for denitrification, shown in Fig. 6 (left panel), reveal the existence of progressively lower O_2 tolerance for step-wise denitrification ($K_{den3}^{o2} < K_{den2}^{o2} < K_{den1}^{o2}$) from all optimized parameter sets. As a result, denitrification can stop at either N_2O or NO_2^- as O_2 increases above anoxic levels, leading to "incomplete" denitrification (Babbin et al., 2015).

Within the anoxic core of the OMZ ($\sim$100 to 350 m depth), O_2 is low enough in all optimizations to allow each of the steps to proceed unimpeded (Fig. 5). The large differences between NO_3^- and NO_2^- reduction (R_{den1} - R_{den2}, middle panel of Fig. 6) allows accumulation of a characteristic subsurface peak in NO_2^- near the OMZ core. Conversely, N_2O produced via NO_2^- reduction (R_{den2}) is quickly consumed via N_2O reduction (R_{den3}) leading to a pronounced N_2O deficit near the OMZ core. The progressive O_2 inhibition of the three steps of denitrification results in a decoupling between these reactions that is particularly evident in the oxycline layers above and below the OMZ, where N_2O accumulation dominates as N_2O reduction (i.e., consumption) is more strongly inhibited by O_2 than NO_2^- reduction (i.e., N_2O production, right panel of Fig. 6). Thus, the O_2 range defined by K^{o2}_{den2} and K^{o2}_{den3} can be thought of as a N_2O-production "window" that allows net N_2O accumulation in the water column (Babbin et al., 2015). This O_2-driven decoupling of anaerobic reactions is consistent with the observed sequential inhibition of N_2O and N_2 production in incubation experiments (Dalsgaard et al., 2014), although we find O_2 inhibition thresholds that are somewhat higher than suggested by those experimental studies. Conversely, other studies have suggested much higher O_2 inhibition thresholds for anaerobic processes, on the order of several $mmol\ m^{-3}$ (Kalvelage et al., 2011; Ji et al., 2018a).
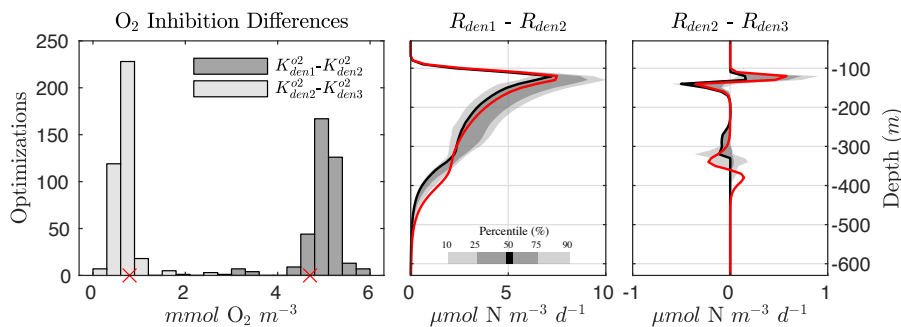
Figure 6. Progressive O_2 inhibition of denitrification steps. (left) Histogram showing the distribution for all optimized solutions of the difference in the O_2 inhibition constant for NO_3^- and NO_2^- reduction (K^{o2}_{den1} and K^{o2}_{den2}, in dark gray), and NO_2^- and N_2O reduction (K^{o2}_{den2} and K^{o2}_{den3}, in light gray). The small red markers denote the values from Opt_{sel}. (middle) Rate differences between NO_3^- and NO_2^- reduction (R_{den1} and R_{den2}). Shading represents the 10/90 and 25/75 percentile at each vertical level from the 382 analyed parameter sets. The bold red curves denote Opt_{sel} results. (right) Same as (middle), but for the difference in NO_2^- and N_2O reduction rates (R_{den2} and R_{den3}).

The vertical profile of the step-wise denitrification rates (R_{den1}, R_{den2}, and R_{den3}) shows remarkable agreement across solutions, with only a small subset of parameter sets that behave as outliers (Fig. 5). As a consequence, the fraction of POC remineralized by each heterotrophic reaction remains consistent across optimizations (Fig. 7, top panels). Near the base of the euphotic zone, around 30 m depth, aerobic remineralization (R_{rem}) far exceeds denitrification, reflecting O_2 inhibition of the latter. However, as O_2 decreases to suboxic levels around 100 m depth, NO_3^- reduction becomes the dominant remineralization pathway (up to 60% of total remineralization). As O_2 drops further within the OMZ core ($\sim$100 to 350 m depth), NO_2^- and N_2O reduction rapidly take up the remaining fraction ($\sim$25% and 15%, respectively), albeit with more variability than near

the euphotic zone. Below the OMZ, as the water column reverts to oxic conditions, aerobic remineralization dominates, and by 500 m depth, all solutions show essentially no denitrification.

410   The processes responsible for fixed N loss (anammox, NO_2^- reduction, and N_2O production from NH_4^+ oxidation) are also consistent across optimizations (Fig. 7, bottom panels). Within oxygenated waters, N_2O production from NH_4^+ oxidation (R_{ao}^{n2o}) is by far the dominant fixed N loss term, as all other sources are inhibited by O_2. Anammox (R_{ax}) becomes the dominant term within the upper and lower oxycline due to increased availability of both NO_2^- (from denitrification and nitrification) and NH_4^+ (from the decomposition of sinking POC), consistent with observations (Babbin et al., 2020). In the anoxic OMZ core,

415   relief from O_2 inhibition allows NO_2^- reduction to outcompete anammox for NO_2^- and contribute up to 60% of the total N loss, with anammox making up the remaining 40% (also see Fig. 5). This is somewhat higher than expected from purely stoichiometric constraints (Koeve and Kähler, 2010; Bianchi et al., 2014), likely reflecting vertical transport of NO_2^- and NH_4^+, co-occurrence of aerobic and anaerobic processes, and the higher O_2 threshold for anammox inhibition in oxygenated waters. The resulting profile of total N loss thus reveals a subsurface maxima predominantly driven by anammox, with denitrification

420   leading total OMZ losses.
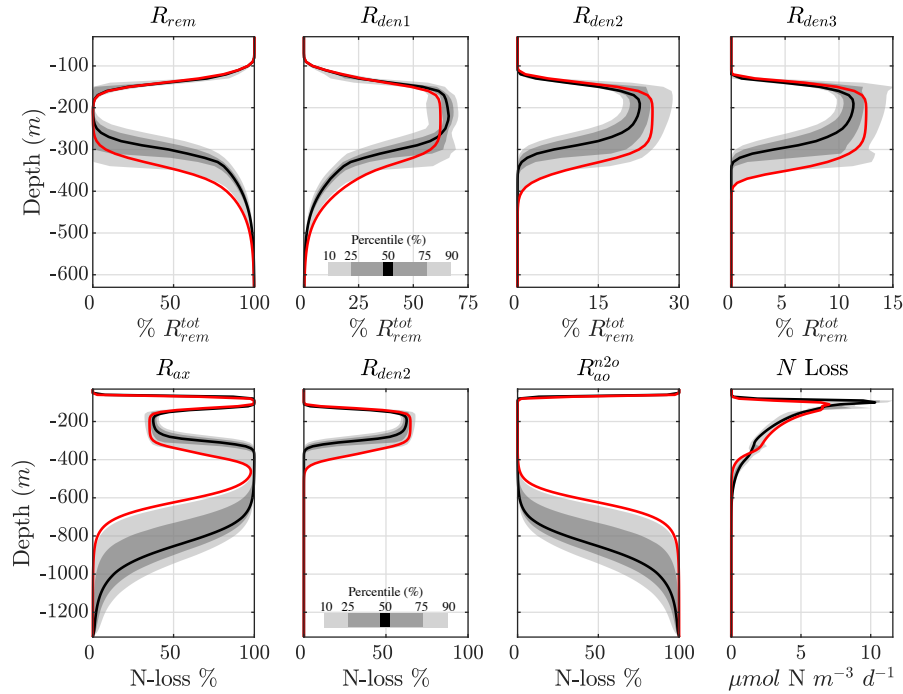
Figure 7. Contribution of different reactions to organic matter remineralization and fixed N loss. (top) Fraction of total POC remineralized by each heterotrophic rate (R_{rem}, R_{den1}, R_{den2}, and R_{den3}). Shading represents the 10/90 and 25/75 percentile at each vertical level from the 382 analyed parameter sets. The bold red curves denote the selected parameter set (Opt_{sel}) discussed in Sect. 5.2. (bottom) Same as (top), but for the fraction of total fixed N loss (via production of N_2 and N_2O) from anammox (R_{ax}), NO_2^- reduction (R_{den2}), and N_2O production from NH_4^+ oxidation (R_{ao}^{n2o}). The total fixed N loss is also shown. Note the different vertical axis for the bottom panels.

5.2 Selected solution for the Eastern Tropical South Pacific

Among tracers, N_2O profiles show significant variability between optimizations. While all optimizations generate two peaks in N_2O surrounding the oxygen deficient core, only a subset is able to reproduce the observed magnitude of the secondary peak at the lower oxycline (roughly 500 m depth, see Fig. 5). This subset forms a "cluster"' of optimizations that share common features that facilitate the formation of a realistic deep N_2O peak, including higher O_2 inhibition thresholds (between 1.0 and 2.0 mmol m^{-3} for NO_2^- reduction, and between 0.5 and 1.0 mmol m^{-3} for N_2O reduction), and a wider O_2 window where net N_2O production is favored (between 0.5 and 1.0 mmol m^{-3} width). Additionally, while most optimizations are able to reproduce the OMZ peak in NO_2^-, significant variability in its magnitude exists. Given the central roles of N_2O and NO_2^- in both nitrification and denitrification pathways (Fig. 1), and the importance of oceanic N_2O emissions to the atmosphere, we assign high priority to optimizations that reproduce realistic features in the distribution of these tracers, in particular a higher magnitude for the secondary N_2O maximum. To this end, we select a parameter set (hereafter Opt_{sel}) which results in N_2O and NO_2^- profiles closer to observations (bold red curves in Fig. 5, with parameter values reported in Table B1). We use this Opt_{sel} parameter set for further analysis of the model sensitivity.

Compared to the other parameter sets, Opt_{sel} is characterized by weaker maximum NH_4^+ and NO_2^- oxidation rates (k_{ao} and k_{no}, respectively) and smaller half saturation constants for reductant uptake (K_{ao}^{nh4} and K_{no}^{no2}, respectively) (Fig. C2). In surface oxygenated waters, this results in relatively higher NH_4^+ and NO_2^- (Fig. 5). In contrast, maximum denitrification rates (k_{den1}, k_{den2}, and k_{den3}) are close to the median values from all optimizations. Rates of NO_2^- and N_2O reduction (R_{den2} and R_{den3}, respectively) are generally larger than other solutions, in particular near the lower oxycline (Fig. 5). This increases POC consumption within this depth range via denitrification compared to other solutions (Fig. 7). As a consequence, the residual between the NO_3^- and NO_2^- reduction (R_{den1} - R_{den2}, see Fig. 6) leads to higher NO_2^- accumulation at these depths, providing the necessary NO_2^- substrate to fuel either NO_2^- reduction (i.e. N_2O production) or anammox. Since the parameterization scheme in Opt_{sel} also results in reduced NO_2^- oxidation (R_{no}) and anammox (R_{ax}) rates (see Fig. 5), likely because of higher anammox half saturation constants for substrate uptake (K_{ax}^{nh4} and K_{ax}^{no2}), more NO_2^- is available for reduction by denitrification, leading to a surplus in production (R_{den2}) relative to consumption (R_{den3}), and high concentrations of N_2O at the lower oxycline.

5.3 Sensitivities to model parameters

As shown in Sect. 5.1 and Fig. 4, strong correlations exist between parameter pairs in the optimization ensemble. Since Opt_{sel} demonstrates good comparisons with ETSP tracer and rate observations, we perform a series of sensitivity tests around parameters (P) most responsible for controlling specific features (F) of the tracer distributions. These include concentrations of NH_4^+ and NO_2^- at 50 m depth, the peak NO_2^- concentration in the OMZ, the N_2O concentrations at the primary and secondary N_2O maxima, and the minimum in the OMZ NO_3^- deficit (i.e., N*). Additionally, we evaluate which parameters govern total N loss, including the fractional contribution of anammox, the partitioning of POC consumption via NO_3^-, NO_2^-, and N_2O reduction, and total N_2O production and air-sea flux (here, approximated by the vertical transport at the upper model boundary). To this

end, we calculated the sensitivity coefficient (ϕ_{ij}) for each P and F pairing by evaluating the impact of varying each Opt_{sel} P value by $\pm 5\%$ of its range in Table B1, and recording the resulting relative change in the F:

$$\phi_{ij} = \frac{P_i}{F_j} \cdot \frac{\partial F_j}{\partial P_i} \tag{12}$$
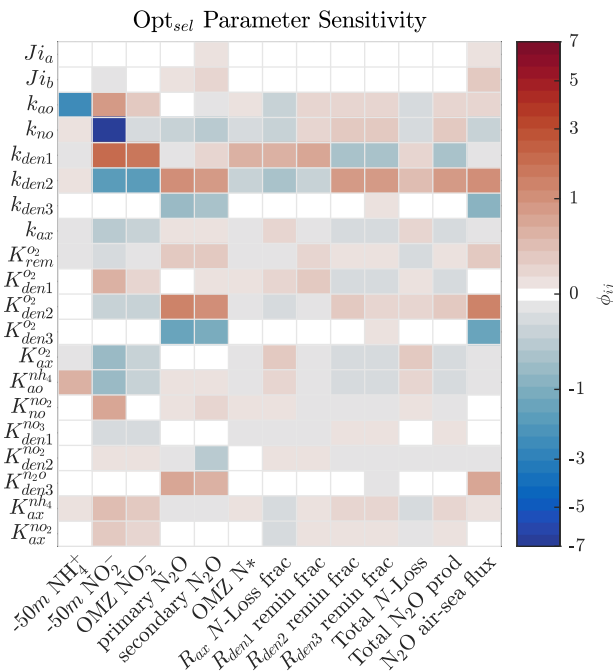
Figure 8. Sensitivity coefficient ($\phi_{ij} = \frac{P_i}{F_j} \cdot \frac{\partial F_j}{\partial P_i}$) for Opt_{sel} parameters (P_i) and features (F_j) of the model solution. Here, each parameter is varied by $\pm 5\%$ of their respective CMA-ES allowed ranges in Table B1 to evaluate the relative impact to each feature of the model solution. Concentrations of NH_4^+ and NO_2^- at 50 m depth (-50 m) are used as proxies of near-surface values.

The results demonstrate high sensitivity to changes in the maximum rates for all reactions (Fig. 8). Specifically, higher maximum rates correlate negatively with the concentrations of their substrates, and positively with the concentrations of their products. For example, increasing k_{den1} results in an increase in OMZ NO_2^-, and a decrease in OMZ N^*. Similarly, increasing k_{den2} decreases OMZ NO_2^- and increases N_2O concentrations in the upper and lower oxycline, and its flux to the atmosphere. These impacts are further modulated by the half saturation and O_2 inhibition constants.

Fig. 9 and 10 further summarize the sensitivities to the maximum denitrification rates and their inhibition by O_2, detailing the resulting changes to O_2, N_2O, NO_2^-, and N^* profiles. As expected, changes in maximum rates affect reaction substrates and products in opposite ways. For example, a positive perturbation of k_{den1} (top panels) stimulates NO_3^- reduction, causing an increase in OMZ NO_2^- and a decrease in N^* as expected. Similarly, a positive perturbation of k_{den2} increases N_2O and decreases NO_2^- nearly everywhere. However, these sensitivities have also specific depth-dependent signatures. While changes

in NO_2^- are more pronounced within the OMZ core, in particular the upper section, changes in N_2O are stronger at the upper and lower oxyclines, i.e., within the N_2O production window defined by K_{den2}^{o2} and K_{den3}^{o2} (see Sect. 5.1).
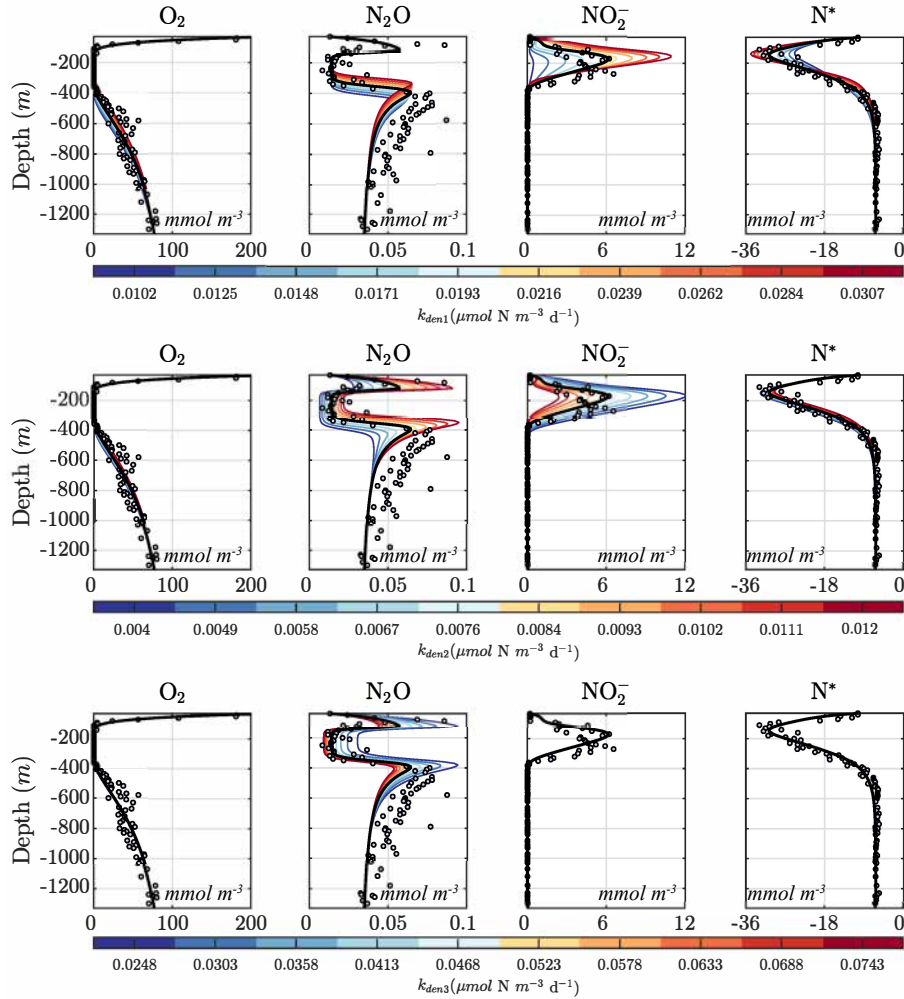
Figure 9. Model sensitivity to parameter values. Panels show O_2, N_2O, NO_2^-, and N^* for the Opt_{sel} parameter set after varying the maximum NO_3^-, NO_2^-, and N_2O reduction rate parameters (k_{den1}, k_{den2}, and k_{den3} by $\pm 5\%$ of their Opt_{sel} value in Table B1.

Notably, by increasing k_{den1} (top panels in Fig. 9) or k_{den2} (middle panels) from Opt_{sel} values, the vertical extent of oxygen
470 deficient waters is reduced as a result of increased POC consumption via denitrification (not shown). This enhances aerobic remineralization and nitrification below the OMZ, providing an enhanced source of NO_3^- that partly offsets the OMZ losses seen via k_{den1} enhancement. This may indicate a potential negative feedback: if denitrification is locally enhanced (i.e. via increased competition for POC by denitrifying heterotrophs), a resulting reduction in the vertical extent of the OMZ would inhibit further N loss.

475   Fig. 8 and 10 highlight significant sensitivities to the O_2 inhibition constants, which control O_2-dependent modulation of the maximum reaction rates. These effects are particularly evident at the boundaries of the OMZ. For example, an increase in K_{den2}^{o2} allows for more NO_2^- reduction at higher O_2, leading to a slight depletion in OMZ NO_2^- and, as a consequence, an increase to suboxic N_2O concentrations (Fig. 10, middle panels), consistent with observations of these processes in the Peruvian oxygen deficient zone (Frey et al., 2020). In a similar manner, an increase in K_{den3}^{o2} leads to more N_2O reduction, 480 reducing the magnitude of both the primary and secondary N_2O peaks, while leaving other OMZ tracers (NO_2^-, N^*) relatively unaffected.
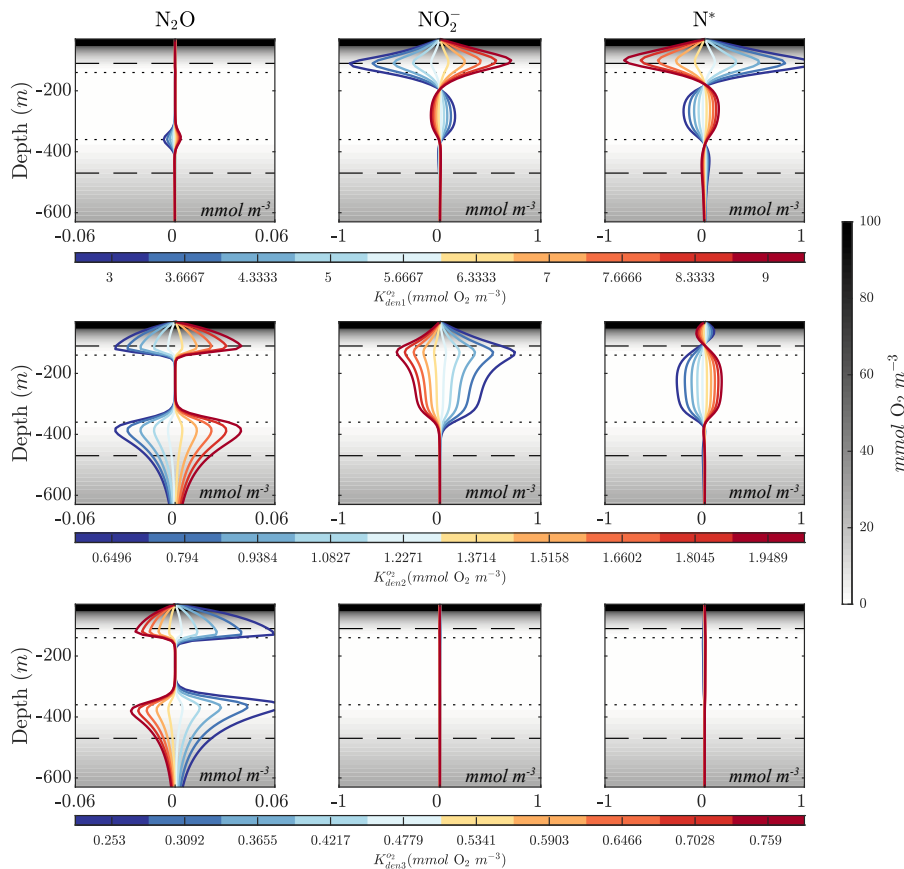
Figure 10. Model sensitivity to parameter values. Panels show changes to N_2O, NO_2^-, and N^* for the Opt_{sel} parameter set after varying the O_2 inhibition constants for NO_3^-, NO_2^-, and N_2O reduction (K_{den1}^{o2}, K_{den2}^{o2}, and K_{den3}^{o2}) by $\pm 5\%$ of their Opt_{sel} value in Table B1. Background gray shadings show O_2 concentrations, with horizontal lines higlighting O_2=1 mmol m^{-3} (dotted lines) and O_2=10 mmol m^{-3} (dashed lines).

5.4 Sensitivities to environmental variables

The main features of the OMZ simulated by the model are strongly dependent on environmental parameters such as upwelling and mixing, organic matter fluxes, and the model boundary conditions, including mixed layer depth and O_2 concentrations. Critically, these parameters are likely to vary over time under the effects of natural climate variability (e.g., Deutsch et al. (2011)), and anthropogenic climate change (Bopp et al., 2013). While each of these parameters control OMZ tracer profiles and N cycle reactions in complex ways, the main responses can be ascribed to changes in the position, thickness, and strength of the anoxic OMZ layer. Perturbations that replenish O_2 above the thresholds for anoxic processes — such as those predicted under climate warming scenarios (Busecke et al., 2022) — have thus cascading impacts on anaerobic N cycle intermediates such as NO_2^- and N_2O, and on the fixed N removal and NO_3^- deficit of the oxygen deficient zone.

Fig. 11 shows the sensitivity of the optimal solution Opt_{sel} to the magnitudes of vertical upwelling (w_{up}) and turbulent diffusion (K_v). Increasing w_{up} results in higher O_2 supply from below the OMZ, leading to increasing O_2 concentrations, and an upward shift and thinning of the anoxic layers. At high upwelling, the anoxic layer is effectively wiped out and is replaced by a suboxic layer. Similar results are obtained with higher K_v values, with an increase of diffusive O_2 supply from both above and below the OMZ, resulting in a progressive shrinking of the anoxic layer. As this layer vanishes, anaerobic processes cease, drastically reducing the concentration of NO_2^- and the N deficit in the OMZ core. Notably, as the OMZ reaches the brink of anoxia, i.e., as the minimum O_2 concentration falls within the N_2O production window, the upper and lower N_2O maxima merge into a single N_2O spike with particularly high N_2O concentrations, reflecting the largest imbalance between production and consumption.

Opposite changes are observed for a reduction in both w_{up} and K_v, which result in an expansion of the OMZ layer, increased NO_3^-, NO_2^-, and N_2O reduction, a larger OMZ NO_2^- peak, and a broader separation of the upper and lower N_2O maxima. The interplay between the position of the oxygen deficient layer, sinking particle fluxes, and transport processes further modulates the response of tracer profiles. For example, as anoxic waters expand upwards following a reduction in K_v, they intercept a higher concentration of sinking organic matter, which in turn fuels higher remineralization rates. Together with reduction in diffusive fluxes, this likely favors the strengthening of the upper N_2O maximum at low K_v observed in Fig. 11.

Because the supply of POC to the OMZ controls the overall magnitude of remineralization reactions, including O_2 consumption and denitrification, the model is particularly sensitive to the sinking POC flux at the upper model boundary (Φ_{poc}^{top}, Table B3; Fig. 12, top panel). Increasing Φ_{poc}^{top} causes a greater remineralization rate, which reduces available O_2, and drives a progressive thickening of the OMZ, with a series of cascading impacts on tracers similar to the ones discussed above. In contrast, decreasing Φ_{poc}^{top} reduces the R_{rem} rates and increases O_2 to the point that anoxic conditions and their signature disappear.

Similar changes can also be driven by variations in the bottom boundary O_2 concentration, which directly controls upward O_2 supply by upwelling (Fig. 12, bottom panel). Increasing bottom O_2 progressively decreases the thickness of the OMZ, shifting it upwards, and eventually eroding the anoxic layer. Conversely, decreasing bottom O_2 leads to a downward expansion of the OMZ and an intensification of anoxic conditions and the resulting anaerobic reactions.
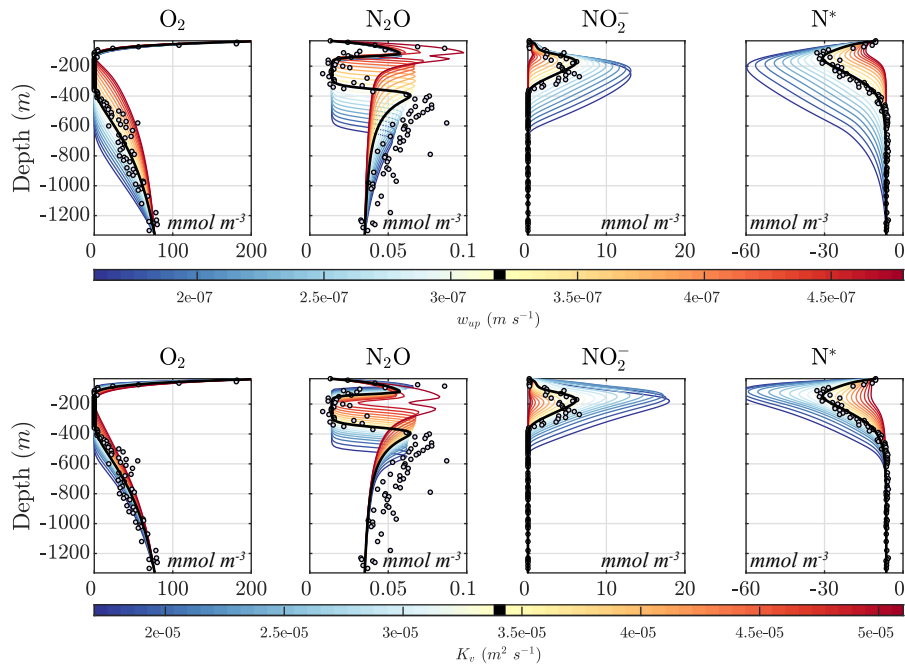
Figure 11. Model sensitivity to physical drivers. (top) Sensitivity of the Opt_{sel} optimized solution to the constant vertical upwelling velocity (w_{up}). (bottom) Sensitivity to the vertical turbulent diffusion coefficient (K_v). The bold black curves indicate original Opt_{sel} values, which are also indicated on their respective colorbars.
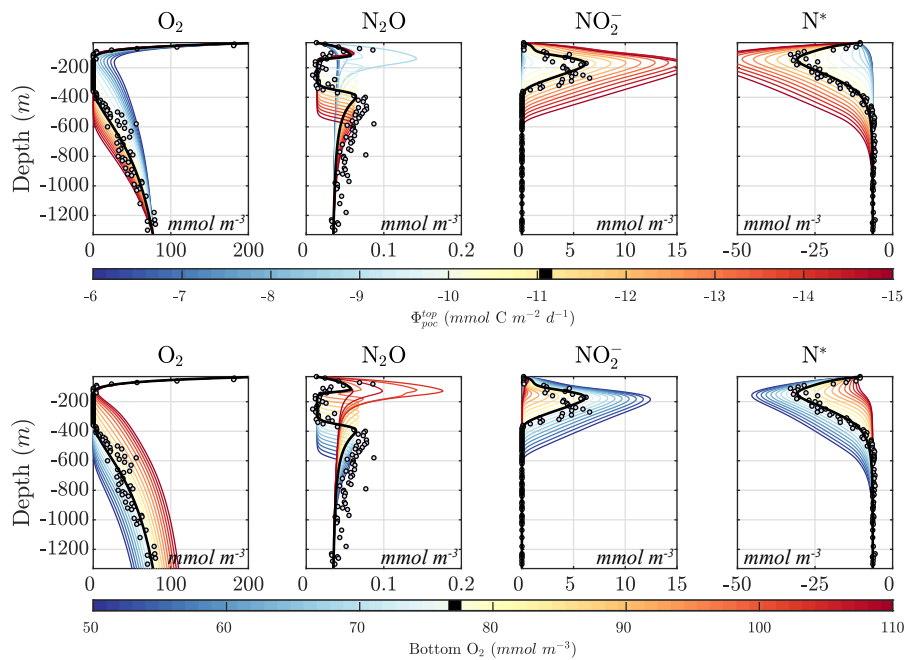
Figure 12. Model sensitivity to biogeochemical drivers. Same as in Fig. 11, but for surface POC flux (Φ_{poc}^{top}) and O_2 concentration at the lower model boundary. In the top panels, more negative values of Φ_{poc}^{top} correspond to an increasing sinking POC flux.

6   Discussion and conclusions

We developed a model of the N cycle in low O_2 waters, and optimized it to reproduce observations from the ETSP OMZ. The model is able to simulate the distribution of multiple N cycle tracers, including NO_2^- and N_2O, and their transformation rates, capturing the underlying dynamics and environmental sensitivity of the underlying reactions (Fig. 5). In general, the model reproduces observed tracer concentration profiles more accuretely than transformation rates. Mismatches with transformation rates may point to processes that need improvement in the model, but also underscore limitations in rate measurements, which rely on shipboard incubation experiments that are usually more uncertain and limited than tracer measurements, and may not perfectly reflect in situ conditions. However, by matching observed reaction rates to a reasonable degree, the model approximates the complex dynamics of the system in a way that allows it to reproduce tracer distributions. Co-located tracer and rate measurements for multiple processes are thus an effective way to constrain the model representation of the N cycle in and around O_2-deficient environments.

The optimization indicates that multiple parameter sets can produce equally good fits to tracer and rate profiles (Fig. 5). This is expected given the non-linear nature of the model, and limitations in the observations. Even when rate measurements are used to constrain the model, as done here, an ensemble of equally good solutions is thus possible. This optimized ensemble shows that significant variability and trade-offs can exist between specific parameters (Fig. 4), suggesting that compensation between different procesess can lead to similar profiles of tracers and transformation rates. Refinements to the criteria used to optimize the model, i.e., additional constraints in the definition of the cost function, could allow to further narrow down plausible sets of parameters. For example, to evaluate the model sensitivity (Fig. 8-10), we select a parameter set from our optimization ensemble that better captures the magnitude of the secondary N_2O maximum, while reproducing other observed features equally well. While we adopt a relatively simple cost function definition, additional constraints such as this one could be explicitly built into its formulation and weighted more heavily to revise model parameters.

A better characterization of environmental sensitivities to substrate concentrations (e.g., half saturation constant for substrate uptake) and O_2 sensitivities would also help parameter selection, for example by narrowing down the prior and posterior range of values for these and other variables (e.g., maximum reaction rates). To this end, rate measurements under a range of O_2 and substrate concentrations are especially helpful. Similarly, simultaneous optimization of the model to reproduce observations across multiple regions of an OMZ characterized by different conditions, e.g., the core and the boundaries, or across different OMZ and oceanographic regimes, would likely result in more robust optimizations.

Despite the variability in parameter values, analysis of the optimal ensemble reveals emerging features that appear robust across multiple optimizations and that compare well with observations. For example, the sensitivity of denitrification processes to O_2 shows systematic variations, with weaker O_2 inhibition for NO_3^- reduction, and stronger for N_2O reduction (Fig. 6). Accordingly, NO_3^- reduction to NO_2^- tends to occur at higher O_2 concentrations than NO_2^- reduction to N_2O, which in turns occurs at higher O_2 concentrations than N_2O reduction to N_2. This result is consistent with tracer incubation experiments (Dalsgaard et al., 2014). However, we note that the specific value of these O_2 sensitivities is far from well-established, with some experiments showing smaller thresholds than found in our optimization (Dalsgaard et al., 2014), and others finding

550 similar or larger thresholds (Ji et al., 2018a). In the model, the sequential sensitivity of denitrification steps to O_2 supports an O_2-dependent window for N_2O production, which allows accumulation of N_2O at the margins of the OMZ core. This, and other systematic relationships between parameters and features of the solutions, as revealed by a sensitivity analysis (Fig. 8-10), shed light on specific balances in the N cycle, and can be exploited as a powerful tool to fine-tune the model, both in the 1D setup used here, and in more complex and resource-intensive 3D implementations where a formal optimization would be 555 unfeasible (McCoy et al., 2022).

Because the model is based on a mechanistic representation of N transformations, it is suitable to investigate the response of the N cycle to environmental variability and other perturbations (Fig. 11-12). For example, the model could be used to investigate the effects of eddy variability near the boundaries of OMZs, or the effects of OMZ expansion and change under global warming. With these goals in mind, the model is designed to be coupled to the biogeochemical component of the current 560 generation of Earth System Models, enabling accurate simulation of NO_2^- and N_2O dynamics, with minimal interference with the representation of the cycles of oxygen, nutrients, carbon, and organic matter.

Because the model reflects an evolving understanding of the N cycle, its assumptions should be re-evaluated as new N transformation processes and aspects of microbial dynamics are uncovered. The model is built around two major simplifications: the "modularity"' of the N cycle, and the representation of microbial metabolisms as "bulk"' chemical reactions that avoid 565 explicitly tracking diverse microbial populations. Both are approximate views of the N cycle. For example, recent evidence suggests that microorganisms with the ability to carry out intracellular reduction of NO_3^- to NO_2^- and NO_2^- to N_2O may dominate production of N_2O in oxygen deficient waters (Ji et al., 2018a; Frey et al., 2020), although the sensitivity of this process to environmental factors is still being uncovered.

Our "bulk"' approach assumes that metabolic reaction rates are proportional to substrates following a Michaelis-Menten 570 dependency. However, in reality, reaction rates also depend on the abundance of microorganisms present in the water column. If microorganism biomass is assumed to be proportional to substrates, then a higher-order dependency of reaction rates may be more appropriate, as adopted by some biogeochemical models (e.g., Paulot et al. (2020)). A different dependence on substrates, in turn, may affect the variability of reaction rates with depth, and the model sensitivity to parameters such as maximum reaction rates.

575 Indeed, previous modeling studies have pointed out the value of explicitly resolving the biomass of microbial populations (Penn et al., 2016; Zakem et al., 2020). This, in turn, enables a more direct comparison of model results with molecular observations (Louca et al., 2016), and would favor the emergence of complex feedbacks between microbes and their substrates driven by resource competition and oceanic circulation (Penn et al., 2019). However, explicitly simulating microbial biomass requires a number of additional parameters that remain poorly constrained and adds computational burden that may not always 580 improve the realism of biogeochemical simulations (Galbraith et al., 2015). Our model provides a valuable framework to continue exploring these ideas in both idealized and realistic settings (McCoy et al., 2022).

Based on its modular design, the model can be naturally expanded to represent new processes that, while thought to be relevant in OMZ, are still uncertain. These include: (1) Additional known N cycle pathways, and their sensitivity to environmental variability, such as DNRA (Lam et al., 2009), hybrid N_2O production from AOA (Stieglmeier et al., 2014), and direct NO_3^-

585 reduction to N_2O (Ji et al., 2018a; Frey et al., 2020); (2) Alternative oxidation pathways, for example NO_2^- oxidation with iodate, or NO_2^- disproportionation reactions (Babbin et al., 2020; Sun et al., 2021a); (3) Coupling of N tracers with the cycles of other elements, e.g. carbon, sulfur and iron, such as chemolithotrophic denitrification coupled to hydrogen sulfide (H_2S) oxidation, or anaerobic NO_2^--based methane (CH_4) oxidation (Azhar et al., 2014; Scholz et al., 2016; Thamdrup et al., 2019; Callbeck et al., 2021); (4) Explict representation of chemolithrotrophy and its effects on organic matter fixation (Swan et al.,
590 2011); (5) Explicit coupling to the inorganic carbon cycle, by inclusion of CO_2 and alkalinity changes associated with N cycle reactions (Cinay et al., 2022); (6) The cycling of nitric oxide (NO) (Ward and Zafiriou, 1988; Lutterbeck et al., 2018); (7) A more detailed representation of the microbial ecology underlying the N cycle (Louca et al., 2016; Zakem et al., 2018; Penn et al., 2019).

Code and data availability. The current version of NitrOMZv1.0 is available from the project website: https://doi.org/10.5281/zenodo.7106213.
595 The exact version of the model used to produce the results used in this paper is archived on Zenodo (Daniele Bianchi, Simon Yang, and Daniel McCoy. (2022). NitrOMZv1.0 Model Code (1.0). Zenodo. https://doi.org/10.5281/zenodo.7106213), as are input data and scripts to run the model and produce the plots for all the simulations presented in this paper (Bianchi et al., 2022).

Author contributions. DB conceptualized the formulation of the model; DB and SY developed the model code, including optimization procedures; DB and SY organized the validation data; DB and DM designed the analyses; DM prepared the tables and visualization of data;
600 DB and DM prepared the manuscript with contributions from SY.

Competing interests. The authors declare that they have no conflict of interest.

Acknowledgements. This material is based upon work supported by the U.S. National Science Foundation under grant OCE-1847687. D.B. acknowledges support from the Alfred P. Sloan Foundation, and computational support by the Extreme Science and Engineering Discovery Environment (XSEDE) through allocation TG-OCE17001. The Authors wish to thank A. Babbin, A. Santoro, C. Kelly for helpful discussion.

Appendix A: NitrOMZ Equations

A1 Heterotrophic rate equations

$$R_{rem} = k_{rem} \cdot \frac{O_2}{K_{rem}^{o2} + O_2} \cdot POC \tag{A1}$$

$$R_{den1} = k_{den1} \cdot \frac{NO_3^-}{K_{den1}^{no3} + NO_3^-} \cdot e^{\frac{-O_2}{K_{den1}^{o2}}} \cdot POC \tag{A2}$$

$$R_{den2} = k_{den2} \cdot \frac{NO_2^-}{K_{den2}^{no2} + NO_2^-} \cdot e^{\frac{-O_2}{K_{den2}^{o2}}} \cdot POC \tag{A3}$$

$$R_{den3} = k_{den3} \cdot \frac{N_2O}{K_{den3}^{n2o} + N_2O} \cdot e^{\frac{-O_2}{K_{den3}^{o2}}} \cdot POC \tag{A4}$$

A2 Chemolithotrophic rate equations

$$R_{ao} = k_{ao} \cdot \frac{O_2}{K_{ao}^{o2} + O_2} \cdot \frac{NH_4^+}{K_{ao}^{nh4} + NH_4^+} \tag{A5}$$

$$R_{no} = k_{no} \cdot \frac{O_2}{K_{no}^{o2} + O_2} \cdot \frac{NO_2^-}{K_{no}^{no2} + NO_2^-} \tag{A6}$$

$$R_{ax} = k_{ax} \cdot \frac{NH_4^+}{K_{ax}^{nh4} + NH_4^+} \cdot \frac{NO_2^-}{K_{ax}^{no2} + NO_2^-} \cdot e^{\frac{-O_2}{K_{ax}^{o2}}} \tag{A7}$$

A3 Aerobic N₂O production

Production of N_2O via the nitrification pathway in NitrOMZ (pathway 2b in Fig. 1) is modelled as a by-product of R_{ao} with enhanced yields at lower O_2 concentrations. The partitioning between N_2O and NO_2^- production from R_{ao} is calculated using the function proposed by Nevison et al. (2003), which was derived by fitting measured N_2O and NO_2^- yields (Y_{ao}^{n2o} and Y_{ao}^{no2}, respectively) to oxygen concentrations (Goreau et al., 1980), and re-fit by multiple observations in the Eastern Tropical North and South Pacific OMZ (Ji et al., 2015a, 2018a; Santoro et al., 2021):

$$\frac{Y_{ao}^{n2o}}{Y_{ao}^{no2}} = \left(\frac{Ji_a}{[O_2]} + Ji_b \right) \cdot 0.01 \tag{A8}$$

Nitrification-derived NO_2^- and N_2O production rates (R_{ao}^{no2} and R_{ao}^{n2o} respectively, pathways 2a and 2b in Fig. 1) are therefore represented as:

$$R_{ao}^{n2o} = R_{ao} \cdot Y_{ao}^{n2o}, \tag{A9}$$

$$R_{ao}^{no2} = R_{ao} \cdot Y_{ao}^{no2}. \tag{A10}$$

A4 Stoichiometry

The stoichiometry of heterotrophic redox reactions is based on an electron balance and follows the procedure outlined in Paulmier et al. (2009), under the assumption that the composition of organic matter (POC) follows the average oceanic ratios

from Anderson and Sarmiento (1994): $C_{106}H_{175}O_{42}N_{16}P$. This chemical composition can be arbitrarily adjusted in NitrOMZ.
Accordingly, the NH_4^+ to C and PO_4^{3-} to C ratios during aerobic respiration are:

$$Q_{rem}^{N:C} = \frac{16}{106}, \tag{A11}$$

$$Q_{rem}^{P:C} = \frac{1}{106}. \tag{A12}$$

As a result of the POC composition, a total of 472 electrons are required to oxidize POC to CO_2. With 4 electrons required to reduce O_2 to H_2O, the oxygen to carbon remineralization ratio for aerobic remineralization to NH_4^+ is represented as:

$$Q_{rem}^{O:C} = \frac{472}{106 \cdot 4}, \tag{A13}$$

This yields a respiration quotient of $r_{-O_2:C}$ of 1.11, which is within range of direct chemical measurements of $r_{-O_2:C}$ from Moreno et al. (2020, 2022). For nitrification, the oxygen to nitrogen ratios for NH_4^+ and NO_2^- oxidation (R_{ao} and R_{no}, respectively) are based on the stoichiometry of the relevant redox reactions:

$$Q_{ao}^{O:N} = \frac{3}{2}, \tag{A14}$$

$$Q_{no}^{O:N} = \frac{1}{2}. \tag{A15}$$

For denitrification, 2 electrons are required for each respective reduction step (NO_3^- to NO_2^-, NO_2^- to N_2O, and N_2O to N_2), thus the corresponding ratios are:

$$Q_{den}^{N:C} = \frac{472}{106 \cdot 2} \tag{A16}$$

Finally, for anammox, NH_4^+ and NO_2^- are combined in 1:1 ratios to produce N_2. The above ratios are then applied to the tracer equations in Appendix A5.

A5 Tracer sources-minus-sinks equations

$$\frac{d[\text{POC}]}{dt} = -(R_{rem} + R_{den1} + R_{den2} + R_{den3}) \tag{A17}$$

$$\frac{d[\text{O}_2]}{dt} = (Q_{rem}^{O:C} \cdot R_{rem}) - (Q_{ao}^{O:N} \cdot R_{ao}) - (Q_{no}^{O:N} \cdot R_{no}) \tag{A18}$$

$$\frac{d[\text{NO}_3^-]}{dt} = R_{no} - (Q_{den}^{N:C} \cdot R_{den1}) \tag{A19}$$

$$\frac{d[\text{PO}_4^{3-}]}{dt} = Q_{rem}^{P:C} \cdot (R_{rem} + R_{den1} + R_{den2} + R_{den3}) \tag{A20}$$

$$\frac{d[\text{NH}_4^+]}{dt} = Q_{rem}^{N:C} \cdot (R_{rem} + R_{den1} + R_{den2} + R_{den3}) - (R_{ao} + R_{ax}) \tag{A21}$$

$$\frac{d[\text{NO}_2^-]}{dt} = R_{ao}^{no_2} + Q_{den}^{N:C} \cdot (R_{den1} - R_{den2}) - (R_{no} + R_{ax}) \tag{A22}$$

$$\frac{d[\text{N}_2\text{O}]}{dt} = 0.5 \cdot (R_{ao}^{n_2o} + Q_{den}^{N:C} \cdot R_{den2}) - (Q_{N:C}^{den} \cdot R_{den3}) \tag{A23}$$

$$\frac{d[\text{N}_2]}{dt} = (Q_{den}^{N:C} \cdot R_{den3}) + R_{ax} \tag{A24}$$

$$\tag{A25}$$

Appendix B: NitrOMZ Parameters and Configurations

Table B1. NitrOMZ nitrogen cycle parameters and CMA-ES optimization ranges.

Parameter	Description	Units	CMA-ES Min Value	CMA-ES Max Value	Opt_{sel} ETSP
Ji_a	Nevison et al. (2003) 'a' parameter	N/A	0.0500	0.4000	0.4000
Ji_b	Nevison et al. (2003) 'b' parameter	N/A	0.0500	0.2000	0.2000
k_{rem}	Maximum aerobic respiration rate	d^{-1}	N/A	N/A	0.0800
k_{den1}	Maximum NO_3^- reduction rate	d^{-1}	0.0080	0.0800	0.0205
k_{den2}	Maximum NO_2^- reduction rate	d^{-1}	0.0080	0.0800	0.0080
k_{den3}	Maximum N_2O reduction rate	d^{-1}	0.0080	0.0800	0.0496
k_{ao}	Maximum NH_4^+ oxidation rate	$\mu\text{mol N m}^{-3}\,\text{d}^{-1}$	0.0100	0.5000	0.0167
k_{no}	Maximum NO_2^- oxidation rate	$\mu\text{mol N m}^{-3}\,\text{d}^{-1}$	0.0100	0.5000	0.0118
k_{ax}	Maximum anammox rate	$\mu\text{mol N m}^{-3}\,\text{d}^{-1}$	0.0100	0.5000	0.4411
K_{rem}^{o2}	O_2 half saturation constant for aerobic respiration	$\text{mmol O}_2\,\text{m}^{-3}$	0.0100	1.0000	1.0000
K_{ao}^{nh4}	NH_4^+ half saturation constant for NH_4^+ oxidation	mmol N m^{-3}	0.0100	1.0000	0.5091
K_{ao}^{o2}	O_2 half saturation constant for NH_4^+ oxidation	$\text{mmol O}_2\,\text{m}^{-3}$	N/A	N/A	0.3300
K_{no}^{no2}	NO_2^- half saturation constant for NO_2^- oxidation	mmol N m^{-3}	0.0100	1.0000	0.3053
K_{no}^{o2}	O_2 half saturation constant for NO_2^- oxidation	$\text{mmol O}_2\,\text{m}^{-3}$	N/A	N/A	0.7780
K_{den1}^{no3}	NO_3^- half saturation constant for NO_3^- reduction	mmol N m^{-3}	0.0100	1.0000	1.0000
K_{den2}^{no2}	NO_2^- half saturation constant for NO_2^- reduction	mmol N m^{-3}	0.0100	1.0000	0.0100
K_{den3}^{n2o}	N_2O half saturation constant for N_2O reduction	mmol N m^{-3}	0.0100	0.2000	0.1587
K_{ax}^{nh4}	NH_4^+ half saturation constant for anammox	mmol N m^{-3}	0.1000	1.0000	1.0000
K_{ax}^{no2}	NO_2^- half saturation constant for anammox	mmol N m^{-3}	0.1000	1.0000	1.0000
K_{den1}^{o2}	O_2 exponential inhibition for NO_3^- reduction	$\text{mmol O}_2\,\text{m}^{-3}$	0.0100	6.0000	6.0000
K_{den2}^{o2}	O_2 exponential inhibition for NO_2^- reduction	$\text{mmol O}_2\,\text{m}^{-3}$	0.0100	3.0000	1.2993
K_{den3}^{o2}	O_2 exponential inhibition for N_2O reduction	$\text{mmol O}_2\,\text{m}^{-3}$	0.0100	3.0000	0.5060
K_{ax}^{o2}	O_2 exponential inhibition for anammox	$\text{mmol O}_2\,\text{m}^{-3}$	0.5000	6.0000	6.0000

Table B2. ETSP configuration for optimization routines.

Name	Description	Unit	Value
z^{top}	Minumum model depth	m	-30
z^{bot}	Maximum model depth	m	-1330
w_{up}	Upwelling velocity (constant)	m y^{-1}	10.0562
K_v^{top}	Upper boundary vertical diffusion coefficient	$\text{m}^2 \text{ y}^{-1}$	750.9983
K_v^{bot}	Lower boundary vertical diffusion coefficient	$\text{m}^2 \text{ y}^{-1}$	1072.8547
K_v^{flex}	Variable (sigmoidal) vertical diffusion parameter	m	-250
K_v^{width}	Variable (sigmoidal) vertical diffusion parameter	m	300
Φ^{top}	Initial POC flux @ -30m	$\text{mmol C m}^{-2} \text{ d}^{-1}$	-11.1
k_{rem}	Maximum aerobic remineralization rate	d^{-1}	0.0800
b	Martin coefficient	N/A	-0.7049

Table B3. ETSP boundary conditions.

Tracer	Units	Top	Bottom
O_2	mmol m^{-3}	225.00	77.00
NO_3^-	mmol m^{-3}	2.81	42.50
PO_4^{3-}	mmol m^{-3}	0.82	3.06
N_2O	µmol m^{-3}	13.00	35.00
NO_2^-	mmol m^{-3}	0.15	0.00
NH_4^+	mmol m^{-3}	0.40	0.00
N_2	mmol m^{-3}	2.00	6.00

Table B4. Optimized ETSP parameter sets.

Name	Parameter Sets	# of Iterations	Perturbations	Tracer Weights $(O_2, NO_3^-, PO_4^{3-}, N_2O, NH_4^+, NO_2^-, N^*)$	Rate Weights $(R_{ao}^{n2o}, R_{den1}, R_{den2}, R_{ax})$
optVK$_v$-v6	45	40k	20%	2, 1, 1, 6, 2, 4, 4	1, 1, 1, 1
optVK$_v$-v7	69	40k	20%	2, 1, 1, 8, 0, 4, 4	1, 1, 1, 1
optVK$_v$-v8	110	40k	20%	2, 1, 1, 12, 2, 4, 4	1, 1, 1, 1
optVK$_v$-v9	158	40k	20%	2, 1, 1, 12, 2, 8, 4	1, 1, 1, 1

Appendix C: Supplemental Figures
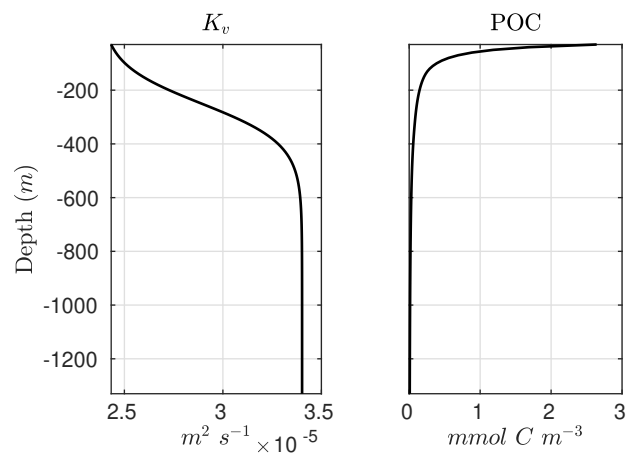
Figure C1. (left) Opt$_{sel}$ vertical diffusion (K_v) and (right) POC profiles.
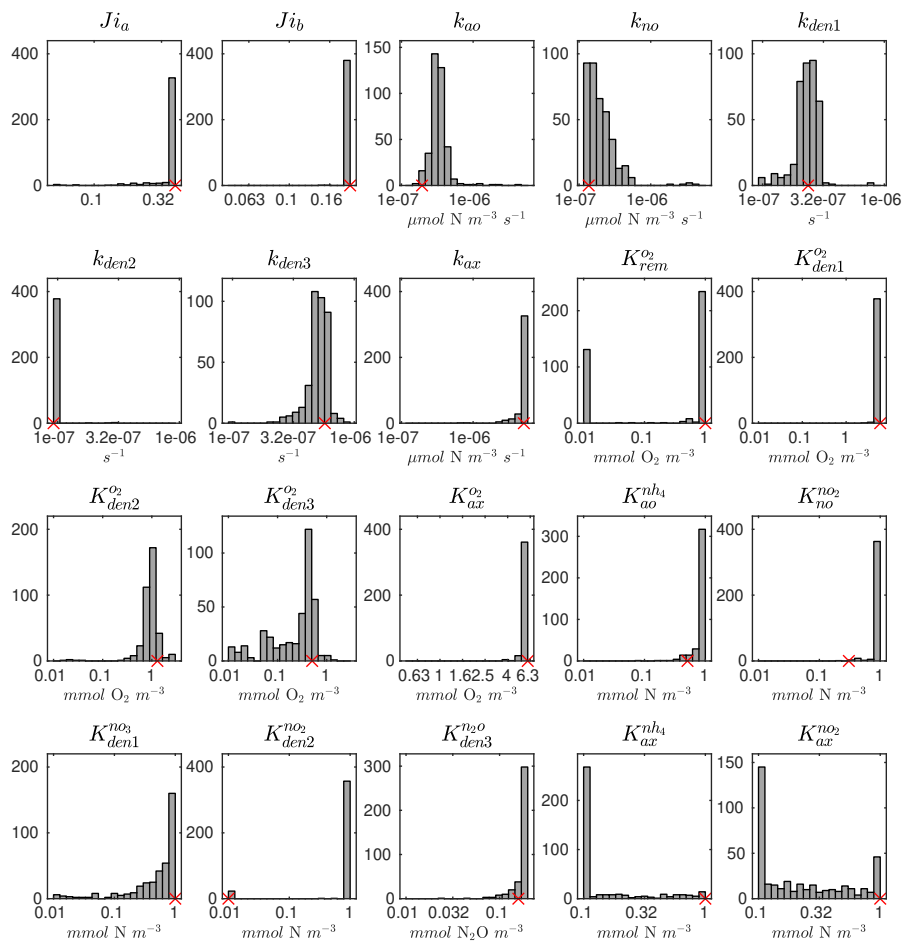
Figure C2. Parameter distributions from the 382 CMA-ES optimized ETSP solutions. Red markers denote Opt$_{sel}$ values.
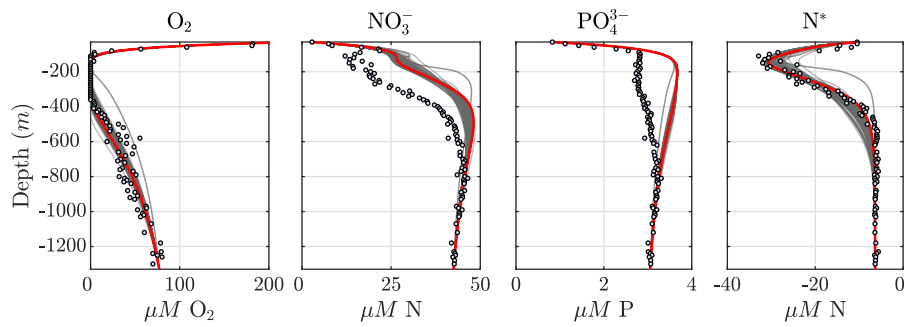
Figure C3. Same as in Figure 5, but for O_2, NO_3^-, PO_4^{3-}, and N∗.

References

635   Anderson, L. A. and Sarmiento, J. L.: Redfield ratios of remineralization determined by nutrient data analysis, Global Biogeochemical Cycles, 8, 65–80, https://doi.org/10.1029/93GB03318, 1994.

Arévalo-Martínez, D. L., Kock, A., Löscher, C. R., Schmitz, R. A., Stramma, L., and Bange, H. W.: Influence of mesoscale eddies on the distribution of nitrous oxide in the eastern tropical South Pacific, Biogeosciences Discussions, 12, 9243–9273, https://doi.org/10.5194/bgd-12-9243-2015, 2015.

640   Aumont, O., Éthé, C., Tagliabue, A., Bopp, L., and Gehlen, M.: PISCES-v2: an ocean biogeochemical model for carbon and ecosystem studies, Geoscientific Model Development, 8, 2465–2513, 2015.

Azhar, M. A., Canfield, D. E., Fennel, K., Thamdrup, B., and Bjerrum, C. J.: A model-based insight into the coupling of nitrogen and sulfur cycles in a coastal upwelling system, Journal of Geophysical Research: Biogeosciences, 119, 264–285, 2014.

Babbin, A. R., Keil, R. G., Devol, A. H., and Ward, B. B.: Organic matter stoichiometry, flux, and oxygen control nitrogen loss in the ocean,
645   Science, 344, 406–408, https://doi.org/10.1126/science.1248364, 2014.

Babbin, A. R., Bianchi, D., Jayakumar, A., and Ward, B. B.: Rapid nitrous oxide cycling in the suboxic ocean, Science, 348, 1127–1129, https://doi.org/10.1126/science.aaa8380, 2015.

Babbin, A. R., Peters, B. D., Mordy, C. W., Widner, B., Casciotti, K. L., and Ward, B. B.: Multiple metabolisms constrain the anaerobic nitrite budget in the Eastern Tropical South Pacific, Global Biogeochemical Cycles, 31, 258–271, https://doi.org/10.1002/2016GB005407, 2017.

650   Babbin, A. R., Buchwald, C., Morel, F. M., Wankel, S. D., and Ward, B. B.: Nitrite oxidation exceeds reduction and fixed nitrogen loss in anoxic Pacific waters, Marine Chemistry, 224, https://doi.org/10.1016/j.marchem.2020.103814, 2020.

Battaglia, G. and Joos, F.: Marine N2O Emissions From Nitrification and Denitrification Constrained by Modern Observations and Projected in Multimillennial Global Warming Simulations, Global Biogeochemical Cycles, 32, 92–121, https://doi.org/10.1002/2017GB005671, 2018.

655   Berelson, W.: The Flux of Particulate Organic Carbon Into the Ocean Interior: A Comparison of Four U.S. JGOFS Regional Studies, Oceanography, 14, 59–67, https://doi.org/10.5670/oceanog.2001.07, 2001.

Bettencourt, J. H., Lopez, C., Hernandez-Garcia, E., Montes, I., Sudre, J., Dewitte, B., Paulmier, A., and Garçon, V.: Boundaries of the Peruvian oxygen minimum zone shaped by coherent mesoscale dynamics, Nature Geoscience, 8, 937–940, https://doi.org/10.1038/ngeo2570, 2015.

660   Bianchi, D., Dunne, J. P., Sarmiento, J. L., and Galbraith, E. D.: Data-based estimates of suboxia, denitrification, and N2O production in the ocean and their sensitivities to dissolved O2, Global Biogeochemical Cycles, 26, https://doi.org/10.1029/2011GB004209, 2012.

Bianchi, D., Babbin, A. R., and Galbraith, E. D.: Enhancement of anammox by the excretion of diel vertical migrators, Proceedings of the National Academy of Sciences, 111, 15 653–15 658, 2014.

Bianchi, D., Weber, T. S., Kiko, R., and Deutsch, C.: Global niche of marine anaerobic metabolisms expanded by particle microenvironments,
665   Nature Geoscience, 11, 263–268, https://doi.org/10.1038/s41561-018-0081-0, 2018.

Bianchi, D., Yang, S., and McCoy, D.: NitrOMZv1.0 Model Code, https://doi.org/10.5281/ZENODO.7106213, 2022.

Bopp, L., Resplandy, L., Orr, J. C., Doney, S. C., Dunne, J. P., Gehlen, M., Halloran, P., Heinze, C., Ilyina, T., Seferian, R., et al.: Multiple stressors of ocean ecosystems in the 21st century: projections with CMIP5 models, Biogeosciences, 10, 6225–6245, 2013.

Boyd, P. W., Claustre, H., Levy, M., Siegel, D. A., and Weber, T.: Multi-faceted particle pumps drive carbon sequestration in the ocean,
670   Nature, 568, 327–335, 2019.

Bristow, L. A., Dalsgaard, T., Tiano, L., Mills, D. B., Bertagnolli, A. D., Wright, J. J., Hallam, S. J., Ulloa, O., Canfield, D. E., Revsbech, N. P., and Thamdrup, B.: Ammonium and nitrite oxidation at nanomolar oxygen concentrations in oxygen minimum zone waters, Proceedings of the National Academy of Sciences of the United States of America, 113, 10 601–10 606, https://doi.org/10.1073/pnas.1600359113, 2016.

675 Buchwald, C., Santoro, A. E., Stanley, R. H., and Casciotti, K. L.: Nitrogen cycling in the secondary nitrite maximum of the eastern tropical North Pacific off Costa Rica, Global Biogeochemical Cycles, 29, 2061–2081, 2015.

Buitenhuis, E. T., Suntharalingam, P., and Le Quéré, C.: Constraints on global oceanic emissions of N 2 O from observations and models, Biogeosciences, 15, 2161–2175, 2018.

Busecke, J. J. M., Resplandy, L., Ditkovsky, S. J., and John, J. G.: Diverging Fates of the Pacific Ocean Oxygen Minimum Zone and Its Core
680 in a Warming World, AGU Advances, 3, https://doi.org/10.1029/2021AV000470, 2022.

Callbeck, C. M., Canfield, D. E., Kuypers, M. M. M., Yilmaz, P., Lavik, G., Thamdrup, B., Schubert, C. J., and Bristow, L. A.: Sulfur cycling in oceanic oxygen minimum zones, Limnology and Oceanography, 66, 2360–2392, https://doi.org/10.1002/lno.11759, 2021.

Capone, D., Bronk, D., Mulholland, M. R., and Carpenter, E.: Nitrogen in the Marine Environment, Elsevier, https://doi.org/10.1016/B978-0-12-372522-6.X0001-1, 2008.

685 Casciotti, K., Forbes, M., Vedamati, J., Peters, B., Martin, T., and Mordy, C.: Nitrous oxide cycling in the Eastern Tropical South Pacific as inferred from isotopic and isotopomeric data, Deep Sea Research Part II: Topical Studies in Oceanography, 156, 155–167, https://doi.org/10.1016/j.dsr2.2018.07.014, 2018.

Cinay, T., Dumit, D., Woosley, R. J., Boles, E. L., Kwiecinski, J. V., Mullen, S., Tamasi, T. J., Wolf, M. J., Kelly, C. L., Travis, N. M., et al.: Coincident biogenic nitrite and pH maxima arise in the upper anoxic layer in the Eastern Tropical North Pacific, Global Biogeochemical
690 Cycles, p. e2022GB007470, 2022.

Dalsgaard, T., Stewart, F. J., Thamdrup, B., De Brabandere, L., Revsbech, N. P., Ulloa, O., Canfield, D. E., and Delong, E. F.: Oxygen at nanomolar levels reversibly suppresses process rates and gene expression in anammox and denitrification in the oxygen minimum zone off Northern Chile, mBio, 5, 1–14, https://doi.org/10.1128/mBio.01966-14, 2014.

De Brabandere, L., Canfield, D. E., Dalsgaard, T., Friederich, G. E., Revsbech, N. P., Ulloa, O., and Thamdrup, B.: Vertical partitioning of
695 nitrogen-loss processes across the oxic-anoxic interface of an oceanic oxygen minimum zone, Environmental Microbiology, 16, 3041–3054, https://doi.org/10.1111/1462-2920.12255, 2014.

Deutsch, C., Brix, H., Ito, T., Frenzel, H., and Thompson, L.: Climate-forced variability of ocean hypoxia, science, 333, 336–339, 2011.

DeVries, T., Deutsch, C., Primeau, F., Chang, B., and Devol, A.: Global rates of water-column denitrification derived from nitrogen gas measurements, Nature Geoscience, 5, 547–550, 2012.

700 DeVries, T., Deutsch, C., Rafter, P. A., and Primeau, F.: Marine denitrification rates determined from a global 3-D inverse model, Biogeosciences, 10, 2481–2496, https://doi.org/10.5194/bg-10-2481-2013, 2013.

Dunne, J. P., Gnanadesikan, A., Sarmiento, J. L., and Slater, R. D.: Technical description of the prototype version (v0) of tracers of phytoplankton with allometric zooplankton (TOPAZ) ocean biogeochemical model as used in the Princeton IFMIP model, Biogeosciences, 7, 3593, 2010.

705 Fasham, M. J. R., Ducklow, H. W., and McKelvie, S. M.: A nitrogen-based model of plankton dynamics in the oceanic mixed layer, Journal of Marine Research, 48, 591–639, https://doi.org/10.1357/002224090784984678, 1990.

Fischer, T., Banyte, D., Brandt, P., Dengler, M., Krahmann, G., Tanhua, T., and Visbeck, M.: Diapycnal oxygen supply to the tropical North Atlantic oxygen minimum zone, Biogeosciences, 10, 5079–5093, 2013.

Frey, C., Bange, H. W., Achterberg, E. P., Jayakumar, A., Löscher, C. R., Arévalo-Martínez, D. L., León-Palmero, E., Sun, M., Sun, X., Xie, R. C., Oleynik, S., and Ward, B. B.: Regulation of nitrous oxide production in low-oxygen waters off the coast of Peru, Biogeosciences, 17, 2263–2287, https://doi.org/10.5194/bg-17-2263-2020, 2020.

Galbraith, E. D., Dunne, J. P., Gnanadesikan, A., Slater, R. D., Sarmiento, J. L., Dufour, C. O., De Souza, G. F., Bianchi, D., Claret, M., Rodgers, K. B., et al.: Complex functionality with minimal computation: Promise and pitfalls of reduced-tracer ocean biogeochemistry models, Journal of Advances in Modeling Earth Systems, 7, 2012–2028, 2015.

Ganesh, S., Bristow, L. A., Larsen, M., Sarode, N., Thamdrup, B., and Stewart, F. J.: Size-fraction partitioning of community gene transcription and nitrogen metabolism in a marine oxygen minimum zone, The ISME Journal, 9, 2682–2696, https://doi.org/10.1038/ismej.2015.44, 2015.

Giovannoni, S. J., Cameron Thrash, J., and Temperton, B.: Implications of streamlining theory for microbial ecology, The ISME Journal, 8, 1553–1565, https://doi.org/10.1038/ismej.2014.60, 2014.

Gnanadesikan, A., Bianchi, D., and Pradal, M. A.: Critical role for mesoscale eddy diffusion in supplying oxygen to hypoxic ocean waters, Geophysical Research Letters, 40, 5194–5198, https://doi.org/10.1002/GRL.50998, 2013.

Goreau, T. J., Kaplan, W. A., Wofsy, S. C., McElroy, M. B., Valois, F. W., and Watson, S. W.: Production of NO(2) and N(2)O by Nitrifying Bacteria at Reduced Concentrations of Oxygen., Applied and environmental microbiology, 40, 526–32, https://doi.org/10.1128/aem.40.3.526-532.1980, 1980.

Graf, D. R., Jones, C. M., and Hallin, S.: Intergenomic comparisons highlight modularity of the denitrification pathway and underpin the importance of community structure for N2O emissions, PloS one, 9, e114 118, 2014.

Gruber, N. and Galloway, J. N.: An Earth-system perspective of the global nitrogen cycle, Nature, 451, 293–296, 2008.

Hansen, N.: The CMA Evolution Strategy: A Comparing Review, in: Towards a New Evolutionary Computation, edited by A., L. J., Larrañaga, P., Iñaki, I., and Endika, B., pp. 75–102, Springer Berlin Heidelberg, Berlin, Heidelberg, https://doi.org/10.1007/3-540-32494-1_4, 2006.

Hansen, N.: The CMA Evolution Strategy: A Tutorial, 2023.

Hansen, N., Niederberger, A., Guzzella, L., and Koumoutsakos, P.: A Method for Handling Uncertainty in Evolutionary Optimization With an Application to Feedback Control of Combustion, IEEE Transactions on Evolutionary Computation, 13, 180–197, https://doi.org/10.1109/TEVC.2008.924423, 2009.

Hooper, A. B. and Terry, K.: Hydroxylamine oxidoreductase of Nitrosomonas, Biochimica et Biophysica Acta (BBA) - Enzymology, 571, 12–20, https://doi.org/10.1016/0005-2744(79)90220-1, 1979.

Jensen, M. M., Lam, P., Revsbech, N. P., Nagel, B., Gaye, B., Jetten, M. S., and Kuypers, M. M.: Intensive nitrogen loss over the Omani Shelf due to anammox coupled with dissimilatory nitrite reduction to ammonium, The ISME Journal, 5, 1660–1670, https://doi.org/10.1038/ismej.2011.44, 2011.

Ji, Q., Babbin, A. R., Jayakumar, A., Oleynik, S., and Ward, B. B.: Nitrous oxide production by nitrification and denitrification in the Eastern Tropical South Pacific oxygen minimum zone, Geophysical Research Letters, 42, 10–755, 2015a.

Ji, Q., Babbin, A. R., Peng, X., Bowen, J. L., and Ward, B. B.: Nitrogen substrate–dependent nitrous oxide cycling in salt marsh sediments, Journal of Marine Research, 73, 71–92, https://doi.org/10.1357/002224015815848820, 2015b.

Ji, Q., Buitenhuis, E., Suntharalingam, P., Sarmiento, J. L., and Ward, B. B.: Global Nitrous Oxide Production Determined by Oxygen Sensitivity of Nitrification and Denitrification, Global Biogeochemical Cycles, 32, 1790–1802, https://doi.org/10.1029/2018GB005887, 2018a.

Ji, Q., Buitenhuis, E., Suntharalingam, P., Sarmiento, J. L., and Ward, B. B.: Global Nitrous Oxide Production Determined by Oxygen Sensitivity of Nitrification and Denitrification, Global Biogeochemical Cycles, 32, 1790–1802, https://doi.org/10.1029/2018GB005887, 2018b.

750 Jin, X. and Gruber, N.: Offsetting the radiative benefit of ocean iron fertilization by enhancing N2O emissions, Geophysical Research Letters, 30, 1–4, https://doi.org/10.1029/2003GL018458, 2003.

Johnson, K. A. and Goody, R. S.: The Original Michaelis Constant: Translation of the 1913 Michaelis–Menten Paper, Biochemistry, 50, 8264–8269, https://doi.org/10.1021/bi201284u, 2011.

Johnston, D. T., Gill, B. C., Masterson, A., Beirne, E., Casciotti, K. L., Knapp, A. N., and Berelson, W.: Placing an upper limit on cryptic
755 marine sulphur cycling, Nature, 513, 530–533, https://doi.org/10.1038/nature13698, 2014.

Kalvelage, T., Jensen, M. M., Contreras, S., Revsbech, N. P., Lam, P., Günter, M., LaRoche, J., Lavik, G., and Kuypers, M. M.: Oxygen sensitivity of anammox and coupled N-cycle processes in oxygen minimum zones, PLoS ONE, 6, https://doi.org/10.1371/journal.pone.0029299, 2011.

Kalvelage, T., Lavik, G., Lam, P., Contreras, S., Arteaga, L., Löscher, C. R., Oschlies, A., Paulmier, A., Stramma, L., and Kuypers,
760 M. M.: Nitrogen cycling driven by organic matter export in the South Pacific oxygen minimum zone, Nature Geoscience, 6, 228–234, https://doi.org/10.1038/ngeo1739, 2013.

Karstensen, J., Stramma, L., and Visbeck, M.: Oxygen minimum zones in the eastern tropical Atlantic and Pacific oceans, Progress in Oceanography, 77, 331–350, https://doi.org/10.1016/j.pocean.2007.05.009, 2008.

Koeve, W. and Kähler, P.: Heterotrophic denitrification vs. autotrophic anammox – quantifying collateral effects on the oceanic carbon cycle,
765 Biogeosciences, 7, 2327–2337, https://doi.org/10.5194/bg-7-2327-2010, 2010.

Kraft, B., Strous, M., and Tegetmeyer, H. E.: Microbial nitrate respiration – Genes, enzymes and environmental distribution, Journal of Biotechnology, 155, 104–117, https://doi.org/10.1016/j.jbiotec.2010.12.025, 2011.

Kriest, I. and Oschlies, A.: On the treatment of particulate organic matter sinking in large-scale models of marine biogeochemical cycles, Biogeosciences, 5, 55–72, https://doi.org/10.5194/bg-5-55-2008, 2008.

770 Kriest, I., Sauerland, V., Khatiwala, S., Srivastav, A., and Oschlies, A.: Calibrating a global three-dimensional biogeochemical ocean model (MOPS-1.0), Geoscientific Model Development, 10, 127–154, https://doi.org/10.5194/gmd-10-127-2017, 2017.

Kuypers, M. M., Marchant, H. K., and Kartal, B.: The microbial nitrogen-cycling network, Nature Reviews Microbiology, 16, 263–276, 2018.

Lam, P. and Kuypers, M. M.: Microbial Nitrogen Cycling Processes in Oxygen Minimum Zones, Annual Review of Marine Science, 3,
775 317–345, https://doi.org/10.1146/annurev-marine-120709-142814, 2011.

Lam, P., Lavik, G., Jensen, M. M., van de Vossenberg, J., Schmid, M., Woebken, D., Gutiérrez, D., Amann, R., Jetten, M. S. M., and Kuypers, M. M. M.: Revising the nitrogen cycle in the Peruvian oxygen minimum zone, Proceedings of the National Academy of Sciences, 106, 4752–4757, https://doi.org/10.1073/pnas.0812444106, 2009.

Long, A. M., Jurgensen, S. K., Petchel, A. R., Savoie, E. R., and Brum, J. R.: Microbial Ecology of Oxygen Minimum Zones Amidst Ocean
780 Deoxygenation, Frontiers in Microbiology, 12, https://doi.org/10.3389/fmicb.2021.748961, 2021a.

Long, M. C., Moore, J. K., Lindsay, K., Levy, M., Doney, S. C., Luo, J. Y., Krumhardt, K. M., Letscher, R. T., Grover, M., and Sylvester, Z. T.: Simulations with the marine biogeochemistry library (marbl), Journal of Advances in Modeling Earth Systems, 13, e2021MS002 647, 2021b.

Löscher, C. R., Kock, A., Könneke, M., Laroche, J., Bange, H. W., and Schmitz, R. A.: Production of oceanic nitrous oxide by ammonia-oxidizing archaea, Biogeosciences, 9, 2419–2429, https://doi.org/10.5194/bg-9-2419-2012, 2012.

Louca, S., Hawley, A. K., Katsev, S., Torres-Beltran, M., Bhatia, M. P., Kheirandish, S., Michiels, C. C., Capelle, D., Lavik, G., Doebeli, M., Crowe, S. A., and Hallam, S. J.: Integrating biogeochemistry with multiomic sequence information in a model oxygen minimum zone, Proceedings of the National Academy of Sciences, 113, https://doi.org/10.1073/pnas.1602897113, 2016.

Lutterbeck, H. E., Arévalo-Martínez, D. L., Löscher, C. R., and Bange, H. W.: Nitric oxide (NO) in the oxygen minimum zone off Peru, Deep Sea Research Part II: Topical Studies in Oceanography, 156, 148–154, https://doi.org/10.1016/j.dsr2.2017.12.023, 2018.

Manizza, M., Keeling, R. F., and Nevison, C. D.: On the processes controlling the seasonal cycles of the air–sea fluxes of O2 and N2O: A modelling study, Tellus B: Chemical and Physical Meteorology, 64, 18 429, 2012.

Martens-Habbena, W., Berube, P. M., Urakawa, H., De La Torre, J. R., and Stahl, D. A.: Ammonia oxidation kinetics determine niche separation of nitrifying Archaea and Bacteria, Nature, 461, 976–979, https://doi.org/10.1038/nature08465, 2009.

Martin, J. H., Knauer, G. A., Karl, D. M., and Broenkow, W. W.: VERTEX: carbon cycling in the northeast Pacific, Deep Sea Research Part A. Oceanographic Research Papers, 34, 267–285, https://doi.org/10.1016/0198-0149(87)90086-0, 1987.

Martinez-Rey, J., Bopp, L., Gehlen, M., Tagliabue, A., and Gruber, N.: Projections of oceanic N2O emissions in the 21st century using the IPSL Earth system model, Biogeosciences, 12, 4133–4148, https://doi.org/10.5194/bg-12-4133-2015, 2015.

McCoy, D., Damien, P., Clements, D. J., Yang, S., and Bianchi, D.: Pathways of Nitrous Oxide Production in the Eastern Tropical South Pacific Oxygen Minimum Zone, Authorea Preprints, https://doi.org/10.22541/essoar.167058932.27589471/v1, 2022.

Moore, J. K., Doney, S. C., and Lindsay, K.: Upper ocean ecosystem dynamics and iron cycling in a global three-dimensional model, Global Biogeochemical Cycles, 18, n/a–n/a, https://doi.org/10.1029/2004GB002220, 2004a.

Moore, J. K., Doney, S. C., and Lindsay, K.: Upper ocean ecosystem dynamics and iron cycling in a global three-dimensional model, Global Biogeochemical Cycles, 18, 2004b.

Moore, J. K., Lindsay, K., Doney, S. C., Long, M. C., and Misumi, K.: Marine Ecosystem Dynamics and Biogeochemical Cycling in the Community Earth System Model [CESM1(BGC)]: Comparison of the 1990s with the 2090s under the RCP4.5 and RCP8.5 Scenarios, Journal of Climate, 26, 9291–9312, https://doi.org/10.1175/JCLI-D-12-00566.1, 2013.

Moreno, A. R., Garcia, C. A., Larkin, A. A., Lee, J. A., Wang, W.-L., Moore, J. K., Primeau, F. W., and Martiny, A. C.: Latitudinal gradient in the respiration quotient and the implications for ocean oxygen availability, Proceedings of the National Academy of Sciences, 117, 22 866–22 872, https://doi.org/10.1073/pnas.2004986117, 2020.

Moreno, A. R., Larkin, A. A., Lee, J. A., Gerace, S. D., Tarran, G. A., and Martiny, A. C.: Regulation of the Respiration Quotient Across Ocean Basins, AGU Advances, 3, https://doi.org/10.1029/2022AV000679, 2022.

Naqvi, S., Bange, H. W., Farías, L., Monteiro, P., Scranton, M., and Zhang, J.: Marine hypoxia/anoxia as a source of CH 4 and N 2 O, Biogeosciences, 7, 2159–2190, 2010.

Nevison, C., Butler, J. H., and Elkins, J. W.: Global distribution of N 2 O and the ΔN 2 O-AOU yield in the subsurface ocean, Global Biogeochemical Cycles, 17, n/a–n/a, https://doi.org/10.1029/2003GB002068, 2003.

Nguyen, T. T., Zakem, E. J., Ebrahimi, A., Schwartzman, J., Caglar, T., Amarnath, K., Alcolombri, U., Peaudecerf, F. J., Hwa, T., Stocker, R., et al.: Microbes contribute to setting the ocean carbon flux by altering the fate of sinking particulates, Nature communications, 13, 1–9, 2022.

Paulmier, A., Kriest, I., and Oschlies, A.: Stoichiometries of remineralisation and denitrification in global biogeochemical ocean models, Biogeosciences, 6, 923–935, https://doi.org/10.5194/bg-6-923-2009, 2009.

Paulot, F., Stock, C., John, J. G., Zadeh, N., and Horowitz, L. W.: Ocean ammonia outgassing: modulation by CO2 and anthropogenic nitrogen deposition, Journal of Advances in Modeling Earth Systems, 12, e2019MS002 026, 2020.

Peng, X., Fuchsman, C. A., Jayakumar, A., Warner, M. J., Devol, A. H., and Ward, B. B.: Journal of Geophysical Research : Oceans

825 Revisiting nitrification in the Eastern Tropical South Pacific : A focus on controls, Journal of Geophysical Research: Oceans, 121, 1667–1684, https://doi.org/10.1002/2015JC011455.Received, 2016.

Penn, J., Weber, T., and Deutsch, C.: Microbial functional diversity alters the structure and sensitivity of oxygen deficient zones, Geophysical Research Letters, 43, 9773–9780, https://doi.org/10.1002/2016GL070438, 2016.

Penn, J. L., Weber, T., Chang, B. X., and Deutsch, C.: Microbial ecosystem dynamics drive fluctuating nitrogen loss in marine anoxic zones,

830 Proceedings of the National Academy of Sciences, 116, 7220–7225, https://doi.org/10.1073/pnas.1818014116, 2019.

Primeau, F.: On the variability of the exponent in the power law depth dependence of POC flux estimated from sediment traps, Deep Sea Research Part I: Oceanographic Research Papers, 53, 1335–1343, 2006.

Santoro, A. E., Buchwald, C., McIlvin, M. R., and Casciotti, K. L.: Isotopic Signature of N_2O Produced by Marine Ammonia-Oxidizing Archaea, Science, 333, 1282–1285, https://doi.org/10.1126/science.1208239, 2011.

835 Santoro, A. E., Buchwald, C., Knapp, A. N., Berelson, W. M., Capone, D. G., and Casciotti, K. L.: Nitrification and Nitrous Oxide Production in the Offshore Waters of the Eastern Tropical South Pacific, Global Biogeochemical Cycles, 35, 1–35, https://doi.org/10.1029/2020GB006716, 2021.

Sarmiento, J. L., Slater, R., Fasham, M., Ducklow, H., Toggweiler, J., and Evans, G.: A seasonal three-dimensional ecosystem model of nitrogen cycling in the North Atlantic euphotic zone, Global biogeochemical cycles, 7, 417–450, 1993.

840 Schartau, M. and Oschlies, A.: Simultaneous data-based optimization of a 1D-ecosystem model at three locations in the North Atlantic: Part I—Method and parameter estimates, Journal of Marine Research, 61, 765–793, https://doi.org/10.1357/002224003322981147, 2003.

Scholz, F., Löscher, C. R., Fiskal, A., Sommer, S., Hensen, C., Lomnitz, U., Wuttig, K., Göttlicher, J., Kossel, E., Steininger, R., and Canfield, D. E.: Nitrate-dependent iron oxidation limits iron transport in anoxic ocean regions, Earth and Planetary Science Letters, 454, 272–281, https://doi.org/10.1016/j.epsl.2016.09.025, 2016.

845 Schreiber, F., Wunderlin, P., Udert, K. M., and Wells, G. F.: Nitric oxide and nitrous oxide turnover in natural and engineered microbial communities: biological pathways, chemical reactions, and novel technologies, Frontiers in Microbiology, 3, https://doi.org/10.3389/fmicb.2012.00372, 2012.

Séférian, R., Berthet, S., Yool, A., Palmieri, J., Bopp, L., Tagliabue, A., Kwiatkowski, L., Aumont, O., Christian, J., Dunne, J., et al.: Tracking improvement in simulated marine biogeochemistry between CMIP5 and CMIP6, Current Climate Change Reports, 6, 95–119, 2020.

850 Smriga, S., Ciccarese, D., and Babbin, A. R.: Denitrifying bacteria respond to and shape microscale gradients within particulate matrices, Communications Biology, 4, 1–9, 2021.

Stein, L. Y. and Yung, Y. L.: Production, Isotopic Composition, and Atmospheric Fate of Biologically Produced Nitrous Oxide, Annual Review of Earth and Planetary Sciences, 31, 329–356, https://doi.org/10.1146/annurev.earth.31.110502.080901, 2003.

Stieglmeier, M., Mooshammer, M., Kitzler, B., Wanek, W., Zechmeister-Boltenstern, S., Richter, A., and Schleper, C.: Aerobic

855 nitrous oxide production through N-nitrosating hybrid formation in ammonia-oxidizing archaea, ISME Journal, 8, 1135–1146, https://doi.org/10.1038/ismej.2013.220, 2014.

Stock, C. A., Dunne, J. P., Fan, S., Ginoux, P., John, J., Krasting, J. P., Laufkötter, C., Paulot, F., and Zadeh, N.: Ocean biogeochemistry in GFDL's Earth System Model 4.1 and its response to increasing atmospheric CO2, Journal of Advances in Modeling Earth Systems, 12, e2019MS002 043, 2020.

860   Sun, X., Ji, Q., Jayakumar, A., and Ward, B. B.: Dependence of nitrite oxidation on nitrite and oxygen in low-oxygen seawater, Geophysical Research Letters, 44, 7883–7891, https://doi.org/10.1002/2017GL074355, 2017.

Sun, X., Frey, C., Garcia-Robledo, E., Jayakumar, A., and Ward, B. B.: Microbial niche differentiation explains nitrite oxidation in marine oxygen minimum zones, The ISME Journal, 15, 1317–1329, https://doi.org/10.1038/s41396-020-00852-3, 2021a.

Sun, X., Jayakumar, A., Tracey, J. C., Wallace, E., Kelly, C. L., Casciotti, K. L., and Ward, B. B.: Microbial N2O consumption in and above
865   marine N2O production hotspots, The ISME Journal, 15, 1434–1444, 2021b.

Suntharalingam, P. and Sarmiento, J. L.: Factors governing the oceanic nitrous oxide distribution: Simulations with an ocean general circulation model, Global Biogeochemical Cycles, 14, 429–454, 2000.

Suntharalingam, P., Buitenhuis, E., Le Quéré, C., Dentener, F., Nevison, C., Butler, J. H., Bange, H. W., and Forster, G.: Quantifying the impact of anthropogenic nitrogen deposition on oceanic nitrous oxide, Geophysical Research Letters, 39,
870   https://doi.org/10.1029/2011GL050778, 2012.

Swan, B. K., Martinez-Garcia, M., Preston, C. M., Sczyrba, A., Woyke, T., Lamy, D., Reinthaler, T., Poulton, N. J., Masland, E. D. P., Gomez, M. L., Sieracki, M. E., DeLong, E. F., Herndl, G. J., and Stepanauskas, R.: Potential for Chemolithoautotrophy Among Ubiquitous Bacteria Lineages in the Dark Ocean, Science, 333, 1296–1300, https://doi.org/10.1126/science.1203690, 2011.

Thamdrup, B., Steinsdóttir, H. G. R., Bertagnolli, A. D., Padilla, C. C., Patin, N. V., Garcia-Robledo, E., Bristow, L. A., and Stewart, F. J.:
875   Anaerobic methane oxidation is an important sink for methane in the ocean's largest oxygen minimum zone, Limnology and Oceanography, 64, 2569–2585, https://doi.org/10.1002/lno.11235, 2019.

Trimmer, M., Chronopoulou, P.-M., Maanoja, S. T., Upstill-Goddard, R. C., Kitidis, V., and Purdy, K. J.: Nitrous oxide as a function of oxygen and archaeal gene abundance in the North Pacific, Nature Communications, 7, 13 451, https://doi.org/10.1038/ncomms13451, 2016.

880   Wang, W.-L., Moore, J. K., Martiny, A. C., and Primeau, F. W.: Convergent estimates of marine nitrogen fixation, Nature, 566, 205–211, https://doi.org/10.1038/s41586-019-0911-2, 2019.

Ward, B. and Zafiriou, O.: Nitrification and nitric oxide in the oxygen minimum of the eastern tropical North Pacific, Deep Sea Research Part A. Oceanographic Research Papers, 35, 1127–1142, https://doi.org/10.1016/0198-0149(88)90005-2, 1988.

Ward, B. A., Friedrichs, M. A., Anderson, T. R., and Oschlies, A.: Parameter optimisation techniques and the problem of underdetermination
885   in marine biogeochemical models, Journal of Marine Systems, 81, 34–43, https://doi.org/10.1016/j.jmarsys.2009.12.005, 2010.

Ward, B. B.: Nitrification in Marine Systems, in: Nitrogen in the Marine Environment, pp. 199–261, Elsevier, https://doi.org/10.1016/B978-0-12-372522-6.00005-0, 2008.

Weber, T. and Bianchi, D.: Efficient particle transfer to depth in oxygen minimum zones of the Pacific and Indian Oceans, Frontiers in Earth Science, 8, 376, 2020.

890   Wrage, N., Velthof, G. L., Van Beusichem, M. L., and Oenema, O.: Role of nitrifier denitrification in the production of nitrous oxide, Soil Biology and Biochemistry, 33, 1723–1732, https://doi.org/10.1016/S0038-0717(01)00096-7, 2001.

Wyrtki, K.: The oxygen minima in relation to ocean circulation, Deep Sea Research and Oceanographic Abstracts, 9, 11–23, https://doi.org/10.1016/0011-7471(62)90243-7, 1962.

Yang, S., Chang, B. X., Warner, M. J., Weber, T. S., Bourbonnais, A. M., Santoro, A. E., Kock, A., Sonnerup, R. E., Bullister, J. L., Wilson,
895   S. T., and Bianchi, D.: Global reconstruction reduces the uncertainty of oceanic nitrous oxide emissions and reveals a vigorous seasonal cycle, Proceedings of the National Academy of Sciences of the United States of America, 117, https://doi.org/10.1073/pnas.1921914117, 2020.

Zakem, E. J., Al-Haj, A., Church, M. J., Van Dijken, G. L., Dutkiewicz, S., Foster, S. Q., Fulweiler, R. W., Mills, M. M., and Follows, M. J.: Ecological control of nitrite in the upper ocean, Nature Communications, 9, https://doi.org/10.1038/s41467-018-03553-w, 2018.

900   Zakem, E. J., Polz, M. F., and Follows, M. J.: Redox-informed models of global biogeochemical cycles, Nature communications, 11, 5680, 2020.